INTERNATIONAL JOURNAL FOR NUMERICAL METHODS IN FLUIDS
Int. J. Numer. Meth. Fluids 2010; **62**:875–905
Published online 6 April 2009 in Wiley InterScience (www.interscience.wiley.com). DOI: 10.1002/fld.2045

Turbulence in a three-dimensional wall-bounded shear flow

A. Holstad[1], H. I. Andersson[2] and B. Pettersen[1,*,†]

[1]*Department of Marine Technology, Norwegian University of Science and Technology, NO-7491 Trondheim, Norway*
[2]*Department of Energy and Process Engineering, Norwegian University of Science and Technology, NO-7491 Trondheim, Norway*

SUMMARY

A new turbulent flow with distinct three-dimensional characteristics has been designed in order to study the impact of mean-flow skewing on the turbulent coherent vortices and Reynolds-averaged statistics. The skewing of a unidirectional plane Couette flow was achieved by means of a spanwise pressure gradient. Direct numerical simulations of the statistically steady Couette–Poiseuille flow enabled in-depth explorations of the turbulence field in the skewed flow. The imposition of a modest spanwise gradient turned the mean flow about 8° away from the original Couette flow direction and this turning angle remained nearly the same over the entire cross section. Nevertheless, a substantial non-alignment between the turbulent shear stress angle and the mean velocity gradient angle was observed. The structure parameter turned out to slightly exceed that in the pure Couette flow, contrary to the observations made in some other three-dimensional shear flows.

Coherent flow structures, which are known to be associated with the Reynolds shear stress in near-wall regions, were identified by the λ_2-criterion. Instantaneous and ensemble-averaged vortices resembled those found in the unidirectional Couette flow. In the skewed flow, however, the vortex structures were turned to align with the local mean-flow direction. The conventional symmetry between Case 1 and Case 2 vortices was broken due to the mean-flow three-dimensionality. The turning of the coherent vortices and the accompanying symmetry-breaking gave rise to secondary and tertiary turbulent shear stress components. By averaging the already ensemble-averaged shear stresses associated with Case 1 and Case 2 vortices in the homogeneous directions, a direct link between the educed near-wall structures and the Reynolds-averaged turbulent stresses was established. These observations provide evidence in support of the hypothesis that the structural model proposed for two-dimensional turbulent boundary layers remains valid also in flows with moderate mean three-dimensionality. Copyright © 2009 John Wiley & Sons, Ltd.

Received 19 September 2008; Revised 5 February 2009; Accepted 8 February 2009

KEY WORDS: near-wall turbulence; mean three-dimensionality; coherent vortices; Couette flow; DNS; structure identification

*Correspondence to: B. Pettersen, Department of Marine Technology, Norwegian University of Science and Technology, NO-7491 Trondheim, Norway.
†E-mail: bjornar@ntnu.no

Contract/grant sponsor: The Research Council of Norway

1. INTRODUCTION

A three-dimensional turbulent boundary layer (3DTBL) is a boundary layer where both the direction and magnitude of the mean flow vary with the distance from the wall. This feature distinguishes a 3DTBL from a two-dimensional turbulent boundary layer (2DTBL), where the direction of the mean flow is independent of the wall distance. The study of 3DTBLs is motivated by the fact that 3DTBLs are commonly encountered in many engineering flows, such as the flow in the bow and stern regions of ships and submarines, as well as in geophysical flows, and also by the fact that the physics of these flows is not well understood. A typical feature of 3DTBLs, especially non-equilibrium ones, is the non-alignment of the turbulent shear stress angle and mean velocity gradient angle in planes parallel to the wall. If the non-alignment is large, turbulence models based on the assumption of an isotropic eddy viscosity will inevitably fail.

3DTBLs can be classified as equilibrium or non-equilibrium, and as pressure-driven or shear-driven flows. In the non-equilibrium (i.e. transient) case, the mean flow is subjected to a rapid change to which the turbulence has not yet adjusted causing the statistical properties of the flow to be non-stationary. In the equilibrium case, on the other hand, the statistical properties of the flow have reached a stationary state. In a pressure-driven flow, the mean three-dimensionality is caused by a mean spanwise pressure gradient, whereas in a shear-driven flow, the three-dimensionality is generated by a moving wall causing a transverse shear. In studies of 3DTBLs, real-life flows are approximated by a combination of these driving mechanisms. Throughout this paper, the terms 3DTBL and 2DTBL will be used also for flows that are strictly wall-bounded shear flows, such as the one considered herein.

3DTBL studies have been reviewed by Bradshaw [1], Eaton [2] and Johnston and Flack [3]. Eaton [2] reviewed several experimental studies focusing on near-wall structures. He concluded that it was probably not possible to define any characteristic structure in a 3DTBL that would adequately describe the wide range of 3DTBL flows. However, all studies indicate that 3DTBLs contain the common features of 2DTBLs, and he therefore argued that the structural model proposed by Robinson [4], and later refined by Jeong *et al.* [5], for 2DTBLs could be used as a basis for 3DTBLs. The studies also indicated that mean three-dimensionality produced an asymmetry in the vortex structures with one sign of vorticity generally weakened relative to the other. Eaton [2] argued that since it is generally believed that the near-wall structures scale on viscous (wall) units and that the height of the peak of the crossflow scales on outer-layer variables, structure distortion would probably be negligible at higher Reynolds numbers.

In their review of several experimental studies, Johnston and Flack [3] raised several important questions related to the changes of near-wall structures due to mean three-dimensionality: (1) Are there equal numbers of positive and negative vortices? (2) Are the total number of vortices reduced or increased due to mean three-dimensionality? (3) Do vortices of opposite sign have different strength, producing stronger or weaker ejections and sweeps? (4) Is mean three-dimensionality important in higher Reynolds number flow? None of these questions were answered, but left open for future studies.

1.1. Non-equilibrium 3DTBLs

Moin *et al.* [6] and Sendstad and Moin [7] approximated a transient 3DTBL by imposing a spanwise pressure gradient on a fully developed channel flow. The flow was studied using direct numerical simulation (DNS). They reported a decrease in the Reynolds stress and a misalignment between

DOI: 10.1002/fld

the shear stress and velocity gradient angles. In addition, the turbulent kinetic energy decreased due to a decrease in the turbulence production combined with an increase in the dissipation. They attributed the reduction of the Reynolds shear stress, turbulent kinetic energy and streamwise mean wall stress to the break-up of the near-wall streaks. The streaks themselves were weakened because the vortices above them were shifted sideways due to the crossflow.

Coleman *et al.* [8] and Le *et al.* [9, 10] approximated their transient 3DTBL, also studied using DNS, by applying an impulsive spanwise motion to the lower wall of a turbulent channel flow. The application of spanwise shear led to a reduction of turbulent kinetic energy and drag, and they attributed this to the mean three-dimensionality breaking up the symmetry and alignment of the near-wall structures, thus disrupting their self-sustaining mechanisms. They also proposed a model for the structural changes based on the model proposed by Jeong *et al.* [5] for 2DTBLs.

Coleman *et al.* [11] studied a transient 3DTBL by subjecting a channel flow to mean strains that approximate the effect of rapid changes in streamwise and spanwise pressure gradients. They concluded that an adverse pressure gradient influences the turbulence far more than pure skewing. They also found that the evolution of the Reynolds shear stress is affected by changes in the velocity–pressure–gradient correlation, and that this term is primarily responsible for the non-alignment of the velocity gradient and shear stress angles.

1.2. Equilibrium 3DTBLs

Bradshaw and Pontikos [12] studied experimentally a 3DTBL approximated by a duct attached to a blower tunnel. A reduction in the magnitude of the shear stress as well as a non-alignment between the shear stress and velocity gradient angles were reported. In order to explain the reduction in the turbulent shear stress, they proposed that the large eddies were tilted sideways by the wall-normal gradient of the mean spanwise velocity component and out of their preferred position and/or orientation. This argument presupposes that the large vortices in a 2DTBL are the most efficient structures for extracting kinetic energy from the mean flow. Schwarz and Bradshaw [13] performed an experimental study by imposing a spanwise pressure gradient using a 30° bend in the horizontal plane. The effects of crossflow were isolated from those of adverse streamwise pressure gradients. The shear stress vector lagged the velocity gradient vector, and the structure parameter was reduced indicating that the crossflow made shear stress production less efficient.

Littell and Eaton [14] investigated experimentally the three-dimensional boundary layer on a rotating disk and reported that the asymmetries in the conditional-sampled shear stress were caused by Reynolds-stress-producing events. They concluded that strong sweeps are caused by streamwise vortices with the same sign as the mean streamwise vorticity (Case 2 structures) and that most strong ejections are caused by streamwise vortices with the opposite sign as the mean streamwise vorticity (Case 1 structures). Finally, they argued that the structural model proposed by Robinson [4] for 2DTBLs could be used as a basis for 3DTBLs. Kang *et al.* [15] also carried out an experiment of an equilibrium 3DTBL over a rotating disk with the objective of investigating the modification of near-wall coherent structures. Asymmetries in the conditional-sampled shear stress were observed, but unlike Littell and Eaton [14] they concluded that the asymmetries were not related to Reynolds-stress-producing events. Flack [16] found that increased mean three-dimensionality did not influence the strength or sign of the streamwise vortices, contrary to the results obtained by Littell and Eaton [14], and in support of the results of Kang *et al.* [15].

Wu and Squires [17] performed a large-eddy-simulation of a turbulent flow over a rotating disk, and obtained results in support of the structural model proposed by Littell and Eaton [14], and also

DOI: 10.1002/fld

reinforced the hypotheses of Littell and Eaton [14] and Johnston and Flack [3] that structural models developed for 2DTBLs can be used for equilibrium 3DTBLs. Lygren and Andersson [18] performed a DNS of the boundary layer flow in a rotor-stator configuration. Near-wall structures were identified by the λ_2-criterion proposed by Jeong and Hussain [19] and ensemble-averaged following the scheme of Jeong *et al.* [5] (λ_2 is the second largest eigenvalue of the tensor $S_{ik}S_{kj}+\Omega_{ik}\Omega_{kj}$ where $S_{ij}=(u_{i,j}+u_{j,i})/2$ is the strain rate tensor and $\Omega_{ij}=(u_{i,j}-u_{j,i})/2$ is the rotation tensor). Quadrant analysis of the conditional-sampled shear stress supported the results by Littell and Eaton [14] and contradicted the results of Kang *et al.* [15] regarding the cause of the asymmetries of the vortices. Jung and Sung [20] carried out a DNS of the 3DTBL in a concentric annulus with a rotating inner cylinder. They discussed the importance of removing the bulk turning effect of the flow, and concluded that aligning the frame of reference with the mean velocity angle and the intensity angle was most appropriate. The value of the structure parameter (defined as the ratio of the magnitude of the shear stresses to twice the turbulent kinetic energy) was larger for the 3DTBL than for their two-dimensional reference case, indicating that the production of turbulent shear stress for a given amount of kinetic energy may be more efficient in a 3DTBL than in a 2DTBL. This behaviour of the structure parameter is opposite of what is normally found in 3DTBLs. They concluded that the three-dimensionality significantly alters the near-wall structure, but that the assumption of Littell and Eaton [14] about the cause of the changes was invalid. The authors concluded that their study indicated that the features of 3DTBLs depend on the flow configuration in question. In two very recent studies, Randriamampianina and Poncet [21] and Poncet and Randriamampianina [22] performed an experimental and numerical (DNS) investigation of turbulence characteristics in an enclosed rotor-stator system. The typical reduction in the structure parameter and the non-alignment of the velocity gradient and turbulent shear stress angles were observed. The results from Lygren and Andersson [18] regarding the role of Case 1 and Case 2 vortices were confirmed. 3DTBLs have also been investigated numerically in references [23–28] and experimentally in [29, 30].

1.3. Present work

Although there are varying reports on the effect of mean three-dimensionality, typical features of 3DTBLs include the non-alignment of the turbulent shear stress angle and mean velocity gradient angle in planes parallel to the wall and the reduction of the structural parameter compared with 2DTBLs. There is also a substantial amount of evidence in support of the hypothesis of Littell and Eaton [14] and Johnston and Flack [3] that structural models developed for 2DTBLs (cf. [4, 5]) can be used for 3DTBLs, and that mean-flow three-dimensionality somehow causes modifications of the near-wall structures. It is not clear, however, exactly how the near-wall structures are modified by the mean three-dimensionality and how these modifications affect the turbulent shear stresses. Most studies have been devoted to only investigating the changes to the primary shear stress component, whereas little attention has been brought to the origin of the secondary and tertiary shear stress components that also exist in 3DTBLs.

One objective of the present study is thus to investigate the origin of the secondary and tertiary shear stress components, and whether, and in what way, these stresses can be related to the same near-wall vortical structures as the primary shear stress component. It is of particular interest to examine if and how global shear stresses can be related to the local flow field surrounding coherent near-wall structures. This will allow us to present evidence supporting or contradicting the hypothesis that the structural model for 2DTBLs can be used also for 3DTBLs. It is also an

DOI: 10.1002/fld

objective to investigate whether, and to what degree, the chosen frame of reference influences the results and conclusions of the structure analysis. To address these issues, an equilibrium three-dimensional skewed Couette/Poiseuille flow is generated and analyzed. The flow will be studied using DNS and the results for the 3DTBL will be compared with a two-dimensional (in the mean) reference case, i.e. the turbulent plane Couette flow.

2. THREE-DIMENSIONAL FLOW CONFIGURATION

2.1. Problem definition

The flow considered in this paper is an equilibrium-skewed Couette/Poiseuille flow which is established by applying a spanwise pressure gradient on an already fully developed turbulent plane Couette flow at $Re = U_w h/\nu = 1300$. The flow configuration is depicted in Figure 1. Here, U_w is half the velocity difference between the walls, h is the channel half-height and ν is the kinematic viscosity of the fluid. $\partial P/\partial y$ is the imposed spanwise pressure gradient driving the crossflow and L_x, L_y and $L_z(=2h)$ are the streamwise, spanwise and wall-normal lengths, respectively. $\tilde{u}$, $\tilde{v}$ and $\tilde{w}$ are the instantaneous velocity components in the streamwise, spanwise and wall-normal directions.

To the best of our knowledge, this flow has never been investigated before, neither numerically nor experimentally. The flow is one of the simplest that produces mean-flow three-dimensionality, is statistically stationary and homogeneous in planes parallel to the walls and reaches an equilibrium state independent of the initial conditions. The numerical configuration is 'clean', clearly set out and easy to understand, which is conducive to companion studies and modelling efforts. The fact that the flow is statistically stationary allows us to distinguish between transient effects (different parts of the flow respond differently to an impulsively started crossflow) and pure three-dimensional effects. There are no complicating effects of wall curvature, adverse pressure gradients and centrifugal forces, and the treatment of boundary and initial conditions is straightforward. In addition, the spanwise velocity gradient is completely decoupled from the streamwise velocity gradient that gives full control of the crossflow.

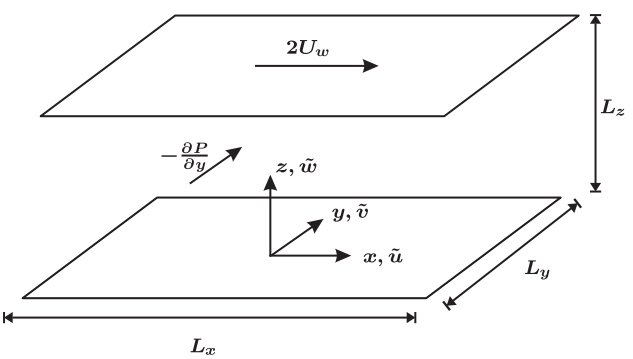

Figure 1. Illustration of flow geometry, coordinate system and computational domain. The mean streamwise (U) and spanwise (V) velocity components are in the positive x- and y-direction, respectively.

DOI: 10.1002/fld

The flow setup is similar to that of Coleman *et al.* [8] and Le *et al.* [9, 10], but they focused solely on the non-equilibrium transition after applying an impulsive motion to the lower wall of a fully developed turbulent plane Poiseuille flow. In the present investigation, the final equilibrium three-dimensional Couette/Poiseuille state is reached in which the direction of the steady mean flow varies with the wall-normal distance. The present flow setup is also similar to that of Jung and Sung [20] who studied three-dimensional effects in a concentric annulus with a rotating inner cylinder. Their case is a generalization of our case since it includes the effects of curvature and centrifugal forces. In the limit of zero curvature, the case of Jung and Sung [20] approaches ours, and it is therefore of great interest to compare results for these two flows. The value of the structure parameter is particularly interesting since Jung and Sung [20], contrary to previous studies, found it to increase throughout the entire near-wall region. Our case and that of Jung and Sung [20] are also as far as we know the only ones where global statistics only depend on one spatial variable, the wall-normal distance, and are independent of time. All other flow cases reported in the literature either depend on two spatial coordinates or one spatial coordinate and on time.

2.2. *Reynolds-averaged Navier–Stokes equations*

Inspection of the simplified RANS (Reynolds-averaged Navier–Stokes)-equations provides us with some valuable insights into the flow even before the results from the simulation are available. Following Tennekes and Lumley [31], and accounting for the stationarity and homogeneity of the mean flow, the RANS-equations can be written as

$$0=\mu\frac{\mathrm{d}^2U}{\mathrm{d}z^2}-\frac{\mathrm{d}(\rho\overline{uw})}{\mathrm{d}z} \tag{1a}$$

$$0=-\frac{\partial P}{\partial y}+\mu\frac{\mathrm{d}^2V}{\mathrm{d}z^2}-\frac{\mathrm{d}(\rho\overline{vw})}{\mathrm{d}z} \tag{1b}$$

$$0=-\frac{\partial P}{\partial z}-\frac{\mathrm{d}(\rho\overline{ww})}{\mathrm{d}z} \tag{1c}$$

All momentum equations are integrable in z, and doing so gives the following result:

$$\tau_{13}=\mu\frac{\mathrm{d}U}{\mathrm{d}z}-\rho\overline{uw}=\text{constant}\equiv\tau_{w_x} \tag{2a}$$

$$\tau_{23}=\mu\frac{\mathrm{d}V}{\mathrm{d}z}-\rho\overline{vw}=\frac{\partial P}{\partial y}z+\text{constant}\equiv\tau_{w_y}\left(1-\frac{z}{h}\right) \tag{2b}$$

$$P+\rho\overline{ww}=-\tau_{w_y}\frac{y}{h}+\text{constant} \tag{2c}$$

An overbar indicates averaging in the homogeneous directions x and y and in time, such that $U=\overline{\tilde{u}}$, $V=\overline{\tilde{v}}$ and $W=\overline{\tilde{w}}=0$ are the mean streamwise, spanwise and wall-normal velocity components. The fluctuating velocity components are defined as $u=\tilde{u}-U$, $v=\tilde{v}-V$ and $w=\tilde{w}-W$. $\tau_{w_x}=\mu\,\mathrm{d}U/\mathrm{d}z|_{z=0}$ and $\tau_{w_y}=\mu\,\mathrm{d}V/\mathrm{d}z|_{z=0}(=-h\partial P/\partial y)$ are the wall shear stresses in x

DOI: 10.1002/fld

and y, μ and ρ are the viscosity and density of the fluid and $-\rho\overline{u_i u_j}$, $1\leqslant i, j\leqslant 3$,[‡] are the turbulent or Reynolds stresses. In this paper, $-\overline{uw}$, $-\overline{vw}$ and $-\overline{uv}$ are referred to as the primary, secondary and tertiary turbulent shear stress, respectively. We see that in the streamwise direction, the total shear stress (viscous and turbulent) τ_{13} will be constant and equal to the wall shear stress τ_{w_x} all across the channel, just as in plane Couette flow (Equation (2a)). In the spanwise direction, the total shear stress τ_{23} will be linearly dependent in z as in plane Poiseuille flow (Equation (2b)). In the wall-normal direction, the sum of P and $\rho\overline{ww}$ will be a function of y since $P=P(y,z)$ (Equation (2c)). The spanwise variation of the mean pressure P results from the imposition of the spanwise pressure gradient, whereas the wall-normal variation of P arises to balance the wall-normal component $-\rho\overline{ww}$ of the Reynolds stress tensor.

The momentum equations in x (Equation (1a)), y (Equation (1b)) and z (Equation (1c)) are seemingly uncoupled, that is no term present in the x momentum equation is present in the y and z momentum equations, and vice versa. The mean momentum equations are, however, coupled implicitly through the Reynolds stress tensor. The Reynolds stress transport equations can provide valuable insight into the relationship between the various components of the Reynolds stress tensor. Following Tennekes and Lumley [31], the transport equations in tensorial form can be written as

$$\frac{\mathrm{D}\overline{u_i u_j}}{\mathrm{D}t} = P_{ij} + D^t_{ij} + D^v_{ij} + \Pi_{ij} - \varepsilon_{ij} \tag{3}$$

where

$$P_{ij} = -(\overline{u_i u_k}\partial U_j/\partial x_k + \overline{u_j u_k}\partial U_i/\partial x_k) \quad \text{(production)} \tag{4a}$$

$$D^t_{ij} = -\partial\overline{u_i u_j u_k}/\partial x_k \quad \text{(turbulent diffusion)} \tag{4b}$$

$$D^v_{ij} = -\nu\partial^2\overline{u_i u_j}/\partial x_k \partial x_k \quad \text{(viscous diffusion)} \tag{4c}$$

$$\Pi_{ij} = \overline{u_i \partial p/\partial x_j} + \overline{u_j \partial p/\partial x_i} \quad \text{(velocity–pressure–gradient correlation)} \tag{4d}$$

$$\varepsilon_{ij} = -2\nu\overline{(\partial u_i/\partial x_k)(\partial u_j/\partial x_k)} \quad \text{(viscous dissipation)} \tag{4e}$$

The nine components of the production term are $P_{11} = -2\overline{uw}\,\mathrm{d}U/\mathrm{d}z$, $P_{12} = P_{21} = -(\overline{uw}\,\mathrm{d}V/\mathrm{d}z + \overline{vw}\mathrm{d}U/\mathrm{d}z)$, $P_{13} = P_{31} = -\overline{ww}\,\mathrm{d}U/\mathrm{d}z$, $P_{22} = -2\overline{vw}\,\mathrm{d}V/\mathrm{d}z$, $P_{23} = P_{32} = -\overline{ww}\,\mathrm{d}V/\mathrm{d}z$ and $P_{33} = 0$. Parts of the Reynolds stress production and the relationship between the stresses are illustrated in Figure 2. The primary shear stress $-\overline{uw}$ is produced by a combination of the normal stress $-\overline{ww}$ and the mean velocity gradient $\mathrm{d}U/\mathrm{d}z$, whereas the secondary shear stress $-\overline{vw}$ is produced by a combination of the normal stress $-\overline{ww}$ and the mean velocity gradient $\mathrm{d}V/\mathrm{d}z$. The normal stress $\overline{uu}$ is produced by $-\overline{uw}$ and $\mathrm{d}U/\mathrm{d}z$, whereas $\overline{vv}$ is produced by $-\overline{vw}$ and $\mathrm{d}V/\mathrm{d}z$. There is no direct production of $\overline{ww}$, but this stress component is caused by the velocity–pressure–gradient correlation, which serves to redistribute energy between the normal stresses. So far, the situation is the same as in a pure Couette flow and a pure Poiseuille flow. The tertiary shear stress $-\overline{uv}$ is produced by the primary and secondary shear stresses and the mean velocity gradients. Since both u and v correlate with w, it is likely that u and v also correlate, causing non-zero $-\overline{uv}$. The tertiary stress does not however enter the RANS-equations due to the homogeneity of the mean

[‡]Here, the notation $\overline{u_i u_j}$, $i, j = 1, 2, 3$, is used for convenience.

DOI: 10.1002/fld

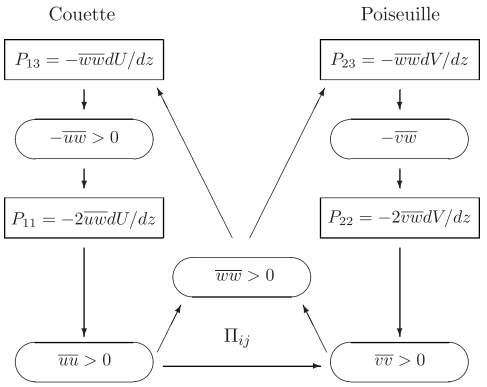

Figure 2. Illustration of parts of the self-sustaining mechanism of turbulence pertinent to the present flow. The boxes illustrate the production terms and the ovals illustrate the turbulent stresses. The contribution from the shear caused by the relative motion between the two walls (Couette) is shown on the left-hand side and the contribution from the mean spanwise pressure gradient (Poiseuille) is shown on the right-hand side.

flow in the streamwise and spanwise directions. This coupling through the Reynolds stress tensor will allow the wall-normal distribution of all turbulent stress components (normal and shear) to be different from what they would be in a plane Couette and Poiseuille flow, respectively.

2.3. Simulation parameters

The initial condition for the skewed 3DTBL Couette/Poiseuille configuration considered in this paper is a fully developed turbulent plane Couette flow at Reynolds number $Re = 1300$, cf. Bech *et al.* [32]. From this initial field, a spanwise pressure gradient is applied and the resulting flow is integrated forward in time until a new statistically stationary state is reached. The transient stage is not investigated.

When performing numerical simulations of this skewed 3DTBL Couette/Poisuille flow, the streamwise wall shear stress and wall friction velocity cannot be estimated beforehand, and the numerical value of τ_{w_x} and $u_{\tau_x} = (\tau_{w_x}/\rho)^{1/2}$ are thus part of the results from the simulation. The spanwise wall shear stress, on the other hand, can be estimated and is related to the spanwise pressure gradient $\tau_{w_y} = \mu \partial V/\partial z|_{z=0} (= -h\partial P/\partial y)$. The spanwise pressure gradient was chosen such that the direction of the mean flow $\beta = \arctan(V/U)$ at the lower wall would settle at between 5° and 10° relative to the x-axis. With the prescribed spanwise pressure gradient, the DNS produced wall shear stresses τ_{w_x} and τ_{w_y} such that their ratio $\tau_{w_y}/\tau_{w_x} = 0.14$. The chosen pressure gradient is not sufficiently large to generate and sustain any turbulent motion on its own, and the turbulence in this flow case is primarily generated by the shear rate caused by the relative motion between the two opposing walls.

3. NUMERICAL PROCEDURES

3.1. Approach for solving the Navier–Stokes equations

The results have been obtained using the computer code MGLET [33], which is based on a finite-volume discretization of the incompressible Navier–Stokes equations. Central differences are used

DOI: 10.1002/fld

Table I. Overview of flow cases.

Case	L_x/h	L_y/h	L_z/h	(N_x, N_y, N_z)	$(\Delta x^+, \Delta y^+)$	Δz^+	Δt^+	Re_τ
Couette	50.24	18.84	2	(768, 288, 192)	(5.40, 5.40)	0.33 − 1.74	0.01313	82.508
3DTBL	50.24	18.84	2	(768, 288, 192)	(5.49, 5.49)	0.34 − 1.76	0.01357	83.975

$N_x(\Delta x^+), N_y(\Delta y^+)$ and $N_z(\Delta z^+)$ are the number of grid points (grid spacing) in the streamwise, spanwise and wall-normal directions. $\Delta x^+ = \Delta x u_\tau/\nu$, $\Delta t^+ = \Delta t u_\tau^2/\nu$, $Re_\tau = u_\tau h/\nu$ and $u_\tau^2 = \sqrt{(\tau_{w_x}^2 + \tau_{w_y}^2)}/\rho$.

for the spatial discretization and the explicit second-order Adams–Bashforth scheme for the time advancement. Periodic boundary conditions are used in the streamwise and spanwise directions, and no-slip boundary conditions are used at the walls. The computational mesh is inhomogeneous in the wall-normal z-direction.

The choice of the size of the computational domain used in the present investigation was based on observations made from the earlier simulation studies by Bech and Andersson [34], Komminaho *et al.* [35], Hu *et al.* [36, 37] and Tsukahara *et al.* [38] in which the domain length and domain width were systematically varied and the results were compared, notably the two-point correlations. We also performed our own parameter study to address this crucial issue [39]. The unanimous conclusion of all these investigations is that a domain length of at least about five times the typical Poiseuille flow domain is required for realistic Couette flow simulations. We have therefore chosen a domain length of approximately $50h$ for the skewed 3DTBL Couette/Poiseuille flow considered in this paper. The grid spacing in the streamwise and spanwise directions is identical to accommodate various degrees of crossflow. Some details of the simulations are shown in Table I.

3.2. DNS database and statistics

The results for the three-dimensional Couette/Poiseuille configuration will be compared with the results for the plane Couette flow (two-dimensional). The DNS database for the three-dimensional case consists of 150 velocity fields sampled every half large-eddy-turnover-time ($t_\tau = h/u_\tau$) after reaching a statistically stationary state, whereas the database in the two-dimensional case consists of 136 velocity fields sampled every quarter large-eddy-turnover-time. This implies that the sampling periods for the three-dimensional case and the two-dimensional case were $75h/u_\tau$ and $34h/u_\tau$, respectively, which is generally considered to be sufficient. Here, u_τ is the wall-friction velocity defined as $u_\tau = (\tau_w/\rho)^{1/2}$ and τ_w is the magnitude of the wall shear stress vector. All results for each flow case are normalized with relevant quantities, e.g. the wall friction velocity, from the same case.

4. MEAN VELOCITIES AND REYNOLDS STRESSES

No other numerically generated or experimental data are available for this three-dimensional flow. Our own two-dimensional case will be used as a reference case, along with some results reported in Bech *et al.* [32]. The mean velocities are shown in Figure 3. At this pressure gradient, the differences between the two-dimensional and three-dimensional flows for the streamwise mean velocity component U are nearly negligible, although the turbulent shear stress $-\overline{uw}$, and thus U through Equation (1a), will be affected by the presence of crossflow due to the coupling of the

DOI: 10.1002/fld

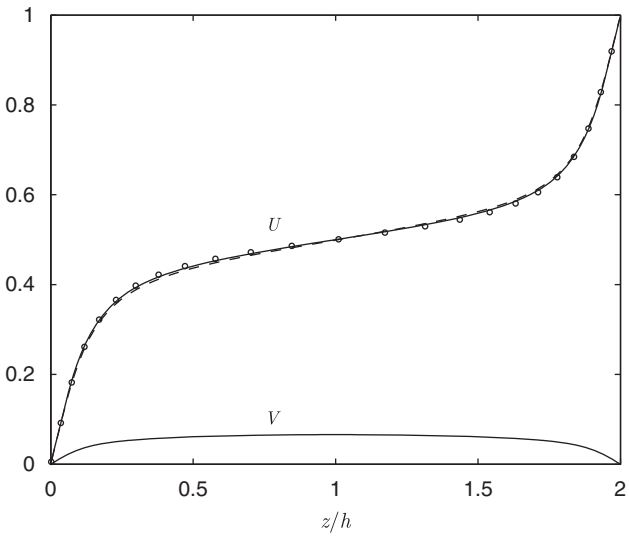

Figure 3. Wall-normal distribution of mean streamwise and spanwise velocity for the 3D case (—), the 2D case (○) and from Bech *et al.* [32] (- - -).

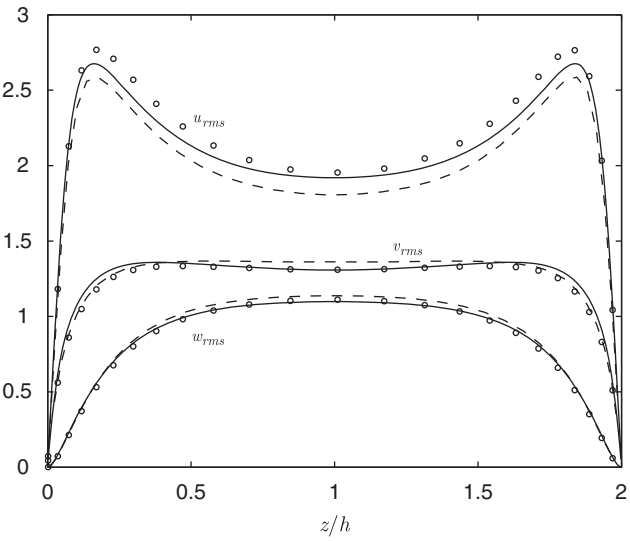

Figure 4. Wall-normal distribution of root-mean-square values of fluctuating velocities normalized by u_τ for the 3D case (—), the 2D case (○) and from Bech *et al.* [32] (- - -).

turbulent stress components through the Reynolds stress tensor. The two-dimensional base case is also in close agreement with the data from Bech *et al.* [32]. The spanwise mean velocity component V is parabolic-like as is the case in pure plane Poiseuille flow. The wall-normal variation of the streamwise and spanwise velocity components resembles those reported in Jung and Sung [20]

DOI: 10.1002/fld

except that their azimuthal velocity, corresponding to our streamwise velocity, is asymmetric due to the effects of the centrifugal forces, which arise in their three-dimensional annular flow.

Figure 4 shows the root-mean-square velocity fluctuations normalized by the wall friction velocity u_τ. The corresponding values from Bech *et al.* [32] are also shown for comparison. The differences between our two-dimensional case and Bech *et al.* [32] two-dimensional case are probably due to the differences in domain size. They used a domain size of about $L_x/h=31$ and $L_y/h=12$. The streamwise root-mean-square values are lower for the three-dimensional case than for the two-dimensional case both in the buffer region and at the channel centre. For the spanwise and wall-normal components, the three-dimensional case yields slightly higher values in the buffer region than the two-dimensional case, whereas the difference between the three-dimensional and two-dimensional cases is negligible in the centre region. The intensities shown in Figure 4 are not merely a combination (weighted sum) of the intensities of the plane Poiseuille and Couette flow, but rather bring evidence that the turbulence is indeed affected by the crossflow. The modest peaks observed in the v_{rms}-profile are apparently signatures of the mean-shear production P_{22} due to the imposed Poiseuille flow.

The viscous and turbulent shear stresses are displayed in Figure 5(a) (τ_{13}) and 5(b) (τ_{23} and $-\overline{uv}$). As was observed already by inspecting the integrated RANS-equations (Equations (2)), the total shear stresses τ_{13} and τ_{23} are constant and linearly dependent in z, respectively. At this pressure gradient, the differences between the two-dimensional and three-dimensional flows for $-\overline{uw}$ and $\mathrm{d}U/\mathrm{d}z$ are small or negligible. The peak of the tertiary shear stress $-\overline{uv}$ is located in the buffer layer at $z/h\approx 0.125(z^+\approx 10)$. In Figure 5(b), the tertiary shear stress is normalized by τ_w whereas the secondary shear stress τ_{23} is normalized by τ_{w_y}. If normalized by the same quantity, the tertiary shear stress is actually larger than the secondary shear stress by a factor of about 5 in the buffer region, and is of the same order of magnitude as the primary turbulent shear stress $-\overline{uw}$. The turbulent shear stresses displayed in Figure 5 qualitatively resemble those reported in Jung and Sung [20], except that the latter are somewhat asymmetric due to the rotation of the inner cylinder.

Four characteristic flow angles are displayed in Figure 6 as a function of the wall-normal distance:

$$\beta=\arctan\frac{V}{U} \tag{5a}$$

$$\alpha=\arctan\frac{\mathrm{d}V/\mathrm{d}z}{\mathrm{d}U/\mathrm{d}z} \tag{5b}$$

$$\eta=\arctan\frac{\overline{vw}}{\overline{uw}} \tag{5c}$$

$$\gamma=\arctan\frac{2\overline{uv}}{\overline{uu}-\overline{vv}} \tag{5d}$$

Here β is the mean velocity angle, α is the mean velocity gradient angle, η is the turbulent shear stress angle and γ is the intensity angle. The results in Figure 6 show that for this flow, the direction of the mean flow varies little with increasing distance from the wall, while the non-alignment of the velocity gradient angle α and the turbulent shear stress angle η indicates distinct three-dimensionality. This non-alignment is typical for 3DTBLs and has been observed in both equilibrium and non-equilibrium flows, e.g. Lygren and Andersson [18] and

DOI: 10.1002/fld

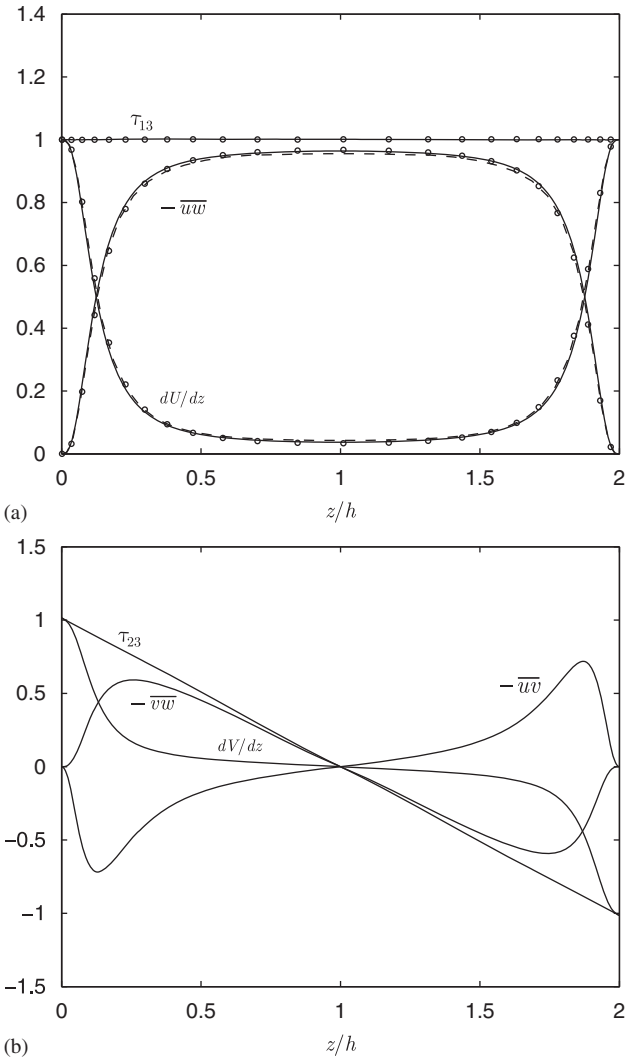

Figure 5. Wall-normal distribution of dimensionless shear stress for the 3D case (—), the 2D case (○) and from Bech *et al.* [32] (- - -): (a) primary shear stress normalized by τ_{w_x} and (b) secondary and tertiary shear stress normalized by τ_{w_y} and τ_w, respectively.

Coleman *et al.* [8]. Turbulence models that are based on an isotropic eddy viscosity will not be suited if the misalignment between the shear stress angle and velocity gradient angle is large. Johnston and Flack [3] concluded that if the misalignment between the turbulent and viscous shear stress components was less than 10°, the errors in assuming an isotropic eddy viscosity should be less than 2–3%. For the weakly skewed flow considered in the present study, the maximum misalignment is quite small ($\alpha-\eta<4°$) and the errors caused by an isotropic eddy viscosity should be acceptable, at least from an engineering point of view. The results for the mean velocity angle

DOI: 10.1002/fld

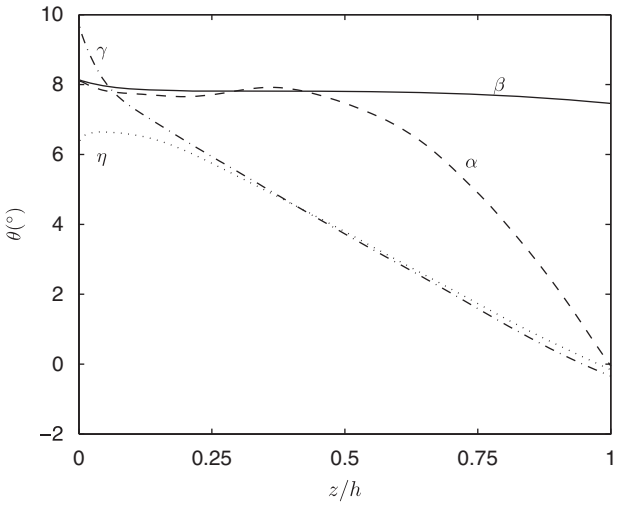

Figure 6. Wall-normal distribution of the mean velocity angle β, the mean velocity gradient angle α, the turbulent shear stress angle η and the intensity angle γ defined in Equation (5). Only the lower half of the channel ($0 \leqslant z/h \leqslant 1$) is shown.

β shown in Figure 6 are in qualitative agreement with the results of Jung and Sung [20] who also found that the dependence of the mean-flow direction on the wall-normal distance was modest. For larger pressure gradients (not shown here), the linear dependence of the mean-flow direction on the wall-normal distance is more evident.

Close to the wall, the turbulent shear stresses $-uw$ and $-vw$ both scale as $\sim z^3$ as can be demonstrated from consideration of the no-slip boundary condition and the continuity equation. In Figure 6, the turbulent shear stress angle η has its maximum close to the wall and then drops almost linearly to zero at the channel centre where $-\overline{vw}$ vanishes while $-\overline{uw}$ remains finite. The intensity angle γ expresses the orientation of the principal axis of the planar turbulent stresses in the xy-plane, cf. Le *et al.* [10]. In the present flow, γ decreases linearly with the wall-normal distance except very close to the wall. γ is also larger than β at the wall. It is noteworthy that for large parts of the near-wall region, the intensity angle γ coincides with the turbulent shear stress angle η while the velocity gradient angle α coincides with the mean velocity angle β. This is contrary to Jung and Sung [20] who in their rotating annulus flow found the intensity angle to coincide with the mean velocity angle, and the mean velocity gradient angle to differ from it. Except for the mean velocity gradient angle, both the denominator and the numerator of the flow angles in Equation (5) become zero as the wall is approached, and any inaccuracies in the computation could be amplified. The values of these flow angles close to the wall should therefore be accepted with some reservation.

When studying the effects of crossflow on turbulent near-wall structures, it is of interest to minimize the bulk turning effect on the structures, or at least to investigate and assess whether, and to what degree, the chosen frame of reference influences the results of the structure analysis. Le *et al.* [10] studied the turbulent structures in a frame of reference aligned with the intensity angle γ, but they mainly employed probability density functions and conditional averages at given wall-normal distances for which the intensity angle can be precisely specified. Jung and Sung [20]

DOI: 10.1002/fld

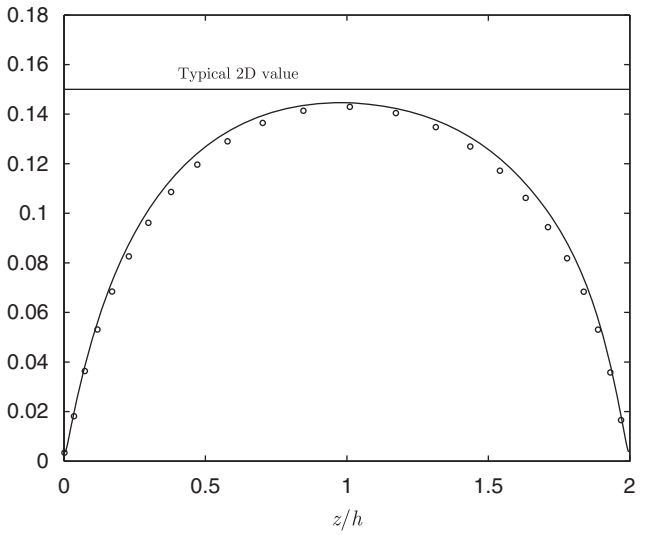

Figure 7. Wall-normal distribution of the structure parameter a_1 for the 3D case (—) and the 2D case (○).

also studied structures in a frame of reference aligned with the intensity angle, but in their flow the variation of the intensity angle with the wall-normal distance was very modest. We intend to study turbulent near-wall structures in the cross-sectional yz-plane and since the variation of the mean velocity angle β with the wall-normal distance z is rather modest, we find it convenient to use a frame of reference aligned with β when assessing the bulk turning effect on the structures. It also seems natural to view the structures in the direction of the local mean flow.

The structure parameter $a_1 = (\overline{uw}^2 + \overline{vw}^2)^{1/2}/(\overline{uu} + \overline{vv} + \overline{ww})$ gives important information about the efficiency of the processes that generate turbulent kinetic energy. In most 3DTBLs, the value of the structure parameter is found to be lower than the typical value of 0.15 in 2DTBLs, cf. Johnston and Flack [3]. Jung and Sung [20], however, found the value a_1 of their 3DTBL to be larger than their two-dimensional reference case throughout the entire near-wall region. They suggested that this increase in the structure parameter was due to the instability associated with the rotation of the inner wall in a concentric annulus, which enables a more efficient extraction of shear stress from a given amount of turbulent kinetic energy. As can be seen from Figure 7, the value of the structure parameter a_1 in our 3DTBL is also larger than that of the two-dimensional reference case, although the difference is more modest than that found by Jung and Sung [20]. This is not surprising since our flow setup and that of Jung and Sung [20] are quite similar. The fact that our case also yields a higher value of the structure parameter does however suggest that the explanation put forward by Jung and Sung [20] about the cause of the increase may be inadequate. It should also be noted that although the value of the structure parameter in our 3DTBL is larger than that of our two-dimensional reference case, they are both lower than the typical value of 0.15 found in most 2DTBLs, whereas Jung and Sung [20] found the value of a_1 to be higher than 0.15 in their 3DTBL and lower in their two-dimensional reference case.

DOI: 10.1002/fld

5. VORTICITY AND COHERENT STRUCTURES

The attention will now be turned towards the details of the near-wall structures in an effort to understand and explain the different statistics of the 3DTBL and the two-dimensional reference case just reported. The vortical structures are extracted using the λ_2 vortex definition proposed by Jeong and Hussain [19] in which a vortex core is defined as a connected region of negative λ_2. Here λ_2 is the second largest eigenvalue of the tensor $S_{ik}S_{kj}+\Omega_{ik}\Omega_{kj}$ where $S_{ij}=(u_{i,j}+u_{j,i})/2$ is the strain rate tensor and $\Omega_{ij}=(u_{i,j}-u_{j,i})/2$ is the rotation tensor. This definition captures the pressure minimum in a plane perpendicular to the vortex axis and, contrary to vorticity-based definitions, also identifies vortex cores in regions with high mean shear. Jeong *et al.* [5] demonstrated that the λ_2 vortex definition is well suited for identifying near-wall structures in turbulent channel flows. Lygren and Andersson [18] and Jung and Sung [20] also used the λ_2 vortex definition in their studies of a stationary 3DTBL.

5.1. *Vorticity and λ_2 statistics*

The wall-normal distributions of the root-mean-square vorticity fluctuations normalized by u_τ^2/ν are presented in Figure 8. The results show that in the buffer region, the streamwise vorticity component ω_x is increased compared with the two-dimensional reference case. This seems to be reasonable since the spanwise pressure gradient will result in a secondary mean strain rate $\mathrm{d}V/\mathrm{d}z$ and consequently higher fluctuations in the spanwise direction, see Figure 4. The spanwise

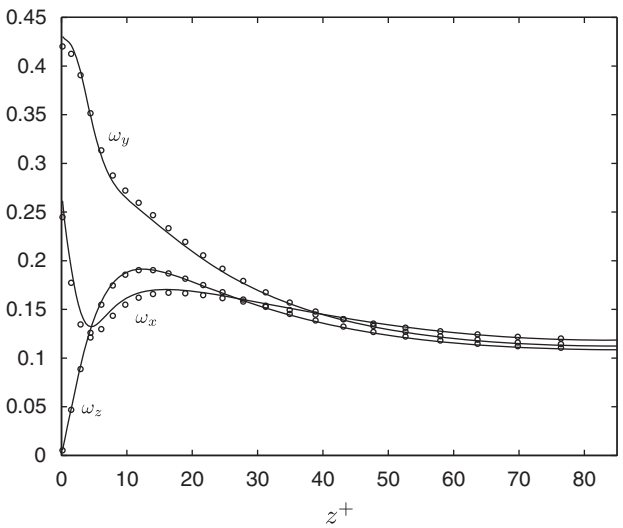

Figure 8. Wall-normal distribution of root-mean-square values of the fluctuating vorticity components normalized by u_τ^2/ν for the 3D case (—) and the 2D case (○). Only the lower half of the channel ($0 \leqslant z^+ \leqslant 84$) is shown.

DOI: 10.1002/fld

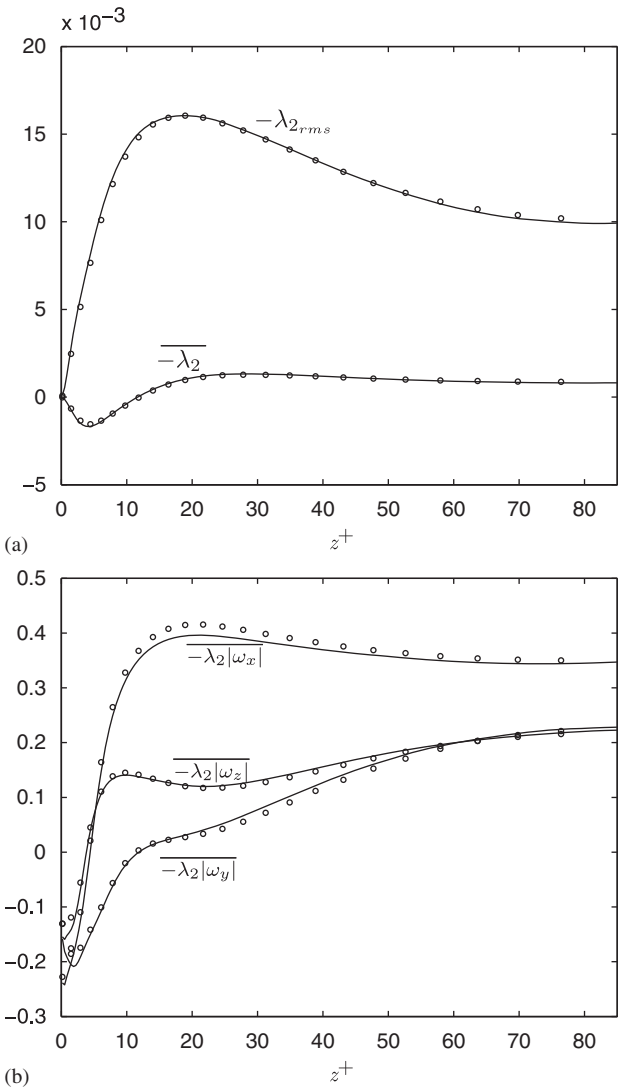

Figure 9. (a) Wall-normal distribution of dimensionless mean and root-mean-square value of $-\lambda_2$ normalized by u_τ^4/ν^2 for the 3D case (—) and the 2D case (○) and (b) wall-normal distribution of dimensionless cross-correlation of $-\lambda_2$ with $|\omega_x|$, $|\omega_y|$ and $|\omega_z|$ for the 3D case (—) and the 2D case (○). Only the lower half of the channel ($0 \leqslant z^+ \leqslant 84$) is shown.

component ω_y is reduced compared with the two-dimensional reference case due to the reduction of the streamwise velocity fluctuations. The wall-normal vorticity component ω_z is more or less unchanged, which is also reasonable since the imposed pressure gradient does not increase the momentum transport in this direction. At the channel centre, the differences between the

DOI: 10.1002/fld

three-dimensional case and the two-dimensional reference case are small or negligible, probably because the gradient $\mathrm{d}V/\mathrm{d}z$ is zero at this location.

Figure 9(a) shows mean and root-mean-square values of $-\lambda_2$ normalized by u_τ^4/v^2 for the three-dimensional case and the two-dimensional case. The mean value is much lower than the root-mean-square value, in fact quite close to zero, across the channel. This implies that regions with negative λ_2 (vortices) are only slightly more probable than regions with positive λ_2 (no vortices). The root-mean-square value gives a better indication of vortical structures than the mean. The peak value of $-\lambda_{2_{\mathrm{rms}}}$ located at $z^+ \approx 20$ indicates that the majority of the structures can be found in the buffer region. Contrary to the plane Poiseuille flow (not shown here), the root-mean-square value $-\lambda_{2_{\mathrm{rms}}}$ for both the three-dimensional case and the two-dimensional reference case exhibits only a modest reduction beyond its peak and settles at the channel centre at a level of about 60% of its maximum level. This suggests that for these flows, vortices may be prominent also in the centre region. The existence of large-scale structures in the core region of the two-dimensional reference case (the plane Couette flow) has been documented in several studies, e.g. Tsukahara *et al.* [38].

The results in Figure 9(a) show that in the buffer region, the difference between the three-dimensional case and the two-dimensional reference case for the root-mean-square value of $-\lambda_2$ is small. The imposed mean pressure gradient causes an increase in the magnitude of the velocity gradients in this region, resulting in higher absolute values of λ_2. Since the values in the three-dimensional case are normalized by the total wall friction velocity $u_\tau = \sqrt{(u_{\tau_x}^2 + u_{\tau_y}^2)}$, the difference becomes small. The fact that the root-mean-square value of $-\lambda_2$ is lower for the three-dimensional case than for the two-dimensional case at the channel centre where the mean velocity gradient $\mathrm{d}V/\mathrm{d}z$ is zero supports this explanation. In the flow case of Jung and Sung [20], the normalization by the total wall friction velocity actually caused the root-mean-square value of $-\lambda_2$ to be smaller for the three-dimensional case than for the two-dimensional reference case. Jung and Sung [20] also reported a significantly higher value for the root-mean-square value of $-\lambda_2$ at the inner wall compared with the two-dimensional case and attributed this to the relatively large mean shear at the inner wall. We find no such increased value at the lower wall. Here, the root-mean-square value for both cases drop off to zero at the lower wall. The mean value of $-\lambda_2$ in Figure 9(a) is more or less unchanged compared with the two-dimensional reference case.

Figure 9(b) shows the cross-correlation between $-\lambda_2$ and each component of the vorticity vector fluctuations. The cross-correlation between two variables a and b is defined as $R = \overline{ab}/(\sqrt{\overline{a^2}}\sqrt{\overline{b^2}})$. The main tendency for both cases is that the cross-correlation between $-\lambda_2$ and $|\omega_x|$ is higher than the cross-correlation between $-\lambda_2$ and $|\omega_y|$ and $|\omega_z|$, thereby indicating that the vortices are predominantly aligned in the streamwise direction. This seems clearly to be the case in the buffer layer, and to some extent also at the channel centre. With respect to the differences between the three-dimensional case and the two-dimensional reference case, we see that in the buffer layer the imposed mean pressure gradient in the three-dimensional case causes $\overline{-\lambda_2|\omega_x|}$ to be reduced as compared with the two-dimensional case. This must imply that for the three-dimensional case, the vortices are somewhat less aligned in the x-direction than in the two-dimensional case. Instantaneous isosurfaces of $-\lambda_2$ normalized by u_τ^4/v^2 in the inner layer for the three-dimensional case (Figure 10) confirm this result. The dominant near-wall structures are elongated (about 200 wall units long) and predominantly oriented in the streamwise direction, as was also seen from Figure 9(b). The vortices are somewhat skewed due to the imposed mean pressure gradient. Vortices with positive ω_x (dark shading) have a different orientation than vortices with negative ω_x (light shading). Apart from that, there are no discernible differences between these instantaneous vortices

DOI: 10.1002/fld

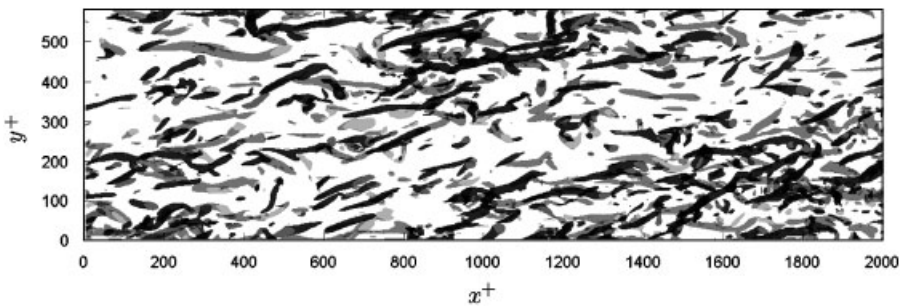

Figure 10. Top view of the isosurfaces of non-dimensional $\lambda_2 = -0.012$ in the range $0 < z^+ < 60$ for the 3D case. The mean flow is from left to right. Dark (light) shading represents positive (negative) streamwise vorticity ω_x. About half of the streamwise length L_x and roughly a third of the spanwise length L_y of the computational domain is shown.

and those of a 2DTBL, see e.g. Jeong *et al.* [5] for a similar plot of instantaneous $-\lambda_2$ isosurfaces for the turbulent plane Poiseuille flow.

5.2. *Ensemble-averaged structures*

The flow field surrounding instantaneous near-wall turbulent vortices will now be ensemble-averaged in order to further investigate the role of the structures. The detection and averaging of the λ_2-structures are based on the scheme devised by Jeong *et al.* [5] that was designed to capture elongated streamwise structures in the near-wall region of a channel flow. The near-wall structures in 3DTBL are expected to be similar to those in 2DTBL. The adequacy of this scheme in identifying near-wall structures in a 3DTBL was verified by Lygren and Andersson [18] and Jung and Sung [20]. A major advantage of using the λ_2 vortex definition is that smearing of the averaged structures is reduced compared with the identification based on velocity and stress signals.

The scheme consists of three steps: (1) to detect vortical structures based on the λ_2-definition conditioned on positive or negative streamwise vorticity ω_x, (2) to ensemble-average the structures by aligning the mid-point of their streamwise length and (3) to maximize the cross-correlation between each individual structure and the ensemble-average by shifting the aligning point of the vortices. Structures having a cross-correlation below 0.5 were discarded to reduce the smearing of the resulting ensemble-averaged structure. The cross-correlation was computed over a box of $150 \times 60 \times 30$ wall units in x, y and z. The structures were also required to have a streamwise length of at least 150 wall units in the region $10 < z^+ < 40$ to capture only fully grown structures. An ensemble-average will be indicated by brackets $\langle\,\rangle$ and the expression $\lambda_2(\langle u_i \rangle)$[§] means that λ_2 is calculated from the ensemble-averaged velocity field.

It is the combined effect of the relative motion of the two parallel walls and the imposed mean pressure gradient that drives the three-dimensional flow considered in this paper. The flow, including the turbulent structures, at the lower and upper wall is therefore identical when the velocity of the upper wall is accounted for. Only structures at the lower half of the channel will therefore be

[§] When referring to ensemble-averaged velocities and stresses, the tildes denoting instantaneous quantities will be omitted for convenience.

DOI: 10.1002/fld

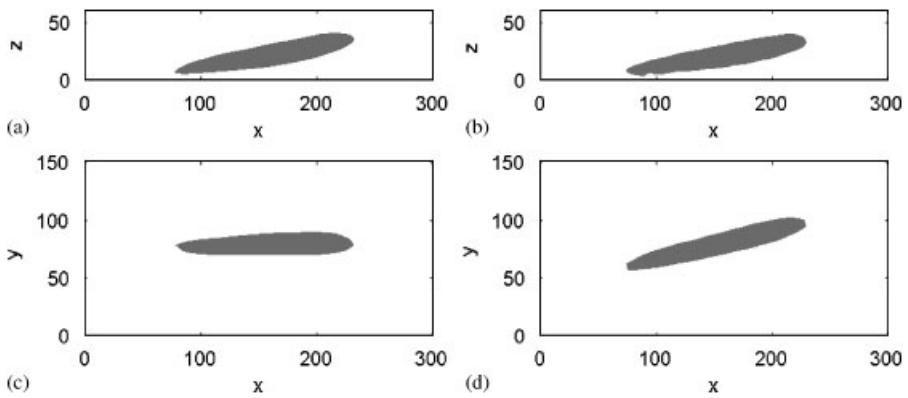

Figure 11. Isosurfaces of ensemble-averaged λ_2-structures in the xyz-frame of reference: (a) side view of structure with negative streamwise vorticity ω_x; (b) with positive ω_x; (c) top view of structure with negative streamwise vorticity ω_x; and (d) with positive ω_x. In this plot x, y and z denote the wall coordinates (normally denoted by x^+, y^+ and z^+) in the streamwise, spanwise and wall-normal directions, respectively.

studied in the following. As discussed in Chapter 4, it is important to assess the bulk turning effect on the structures. Since the global RANS statistics are expressed in the xyz-frame of reference, the educed near-wall structure will primarily also be studied in the xyz-frame of reference in order to be able to discuss the direct relationship between the two. The bulk turning effect on the structures will then be addressed by also aligning the frame of reference with the direction of the mean flow, and comparing the level and distribution of the contour lines of ensemble-averaged velocities and turbulent stresses in the two coordinate systems. The nomenclature of Shizawa and Eaton [40] is adopted to identify vortices of opposite sign; Case 1 vortices have induced near-wall velocity in the direction of the mean crossflow, while Case 2 vortices have induced near-wall velocity in the opposite direction of the mean crossflow.

Figure 11 shows isosurfaces of ensemble-averaged λ_2-structures $\lambda_2(\langle u_i \rangle)$. The direction of the mean flow is from left to right, but the frame of reference is not aligned with the direction of the mean flow. The tilt angles of Case 1 and Case 2 vortices correspond to the observed orientation of dark and light isosurfaces in Figure 10. In Figure 12, on the other hand, the same ensemble-averaged structures are displayed in a frame of reference aligned with the direction of the mean flow. Because the mean three-dimensionality is relatively weak in this case, it is hard to discern any difference between positive and negative structures. An enlarged view does nevertheless reveal some differences. The tilt angles for Case 1 (positive ω_x) and Case 2 (negative ω_x) vortices are about $+6°$ and $-7°$, whereas the inclination angles for positive and negative vortices are about $+8°$ and $+10°$, respectively. Jung and Sung [20] reported the tilt angles for their near-wall structures to be about $+8°$ and $+20°$ for Case 1 and Case 2 vortices, and the inclination angles to be about $+13°$ and $+8°$ for Case 1 and Case 2 vortices. They used a frame of reference aligned with the intensity angle, which in their case almost coincided with the mean velocity angle. Their results should therefore be comparable with ours. The length and diameter of the vortices are about 200 and 25 wall units, in accordance with previous reports, e.g. Jeong *et al.* [5] for a 2DTBL and Lygren and Andersson [18] and Jung and Sung [20] for 3DTBLs.

DOI: 10.1002/fld

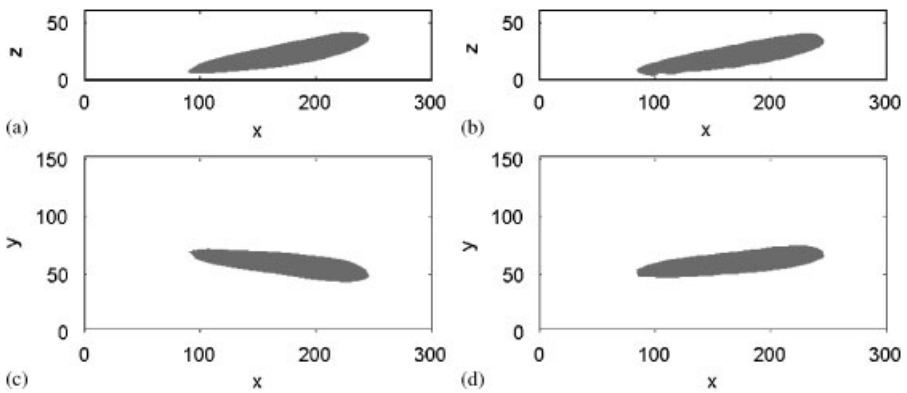

Figure 12. Isosurfaces of ensemble-averaged λ_2-structures in a frame of reference aligned with the direction of the mean flow: (a) side view of structure with negative streamwise vorticity ω_x; (b) with positive ω_x; (c) top view of structure with negative streamwise vorticity ω_x; and (d) with positive ω_x. In this plot x, y and z denote the wall coordinates (normally denoted by x^+, y^+ and z^+) in the streamwise, spanwise and wall-normal directions, respectively.

5.3. Velocities and shear stresses at the vortex midpoint

In the following, ensemble-averaged velocities and turbulent shear stresses are further investigated in an effort to explain the global statistics reported earlier in the paper and also to identify differences and similarities with other equilibrium 3DTBLs. All plots show a cross-sectional cut through the midpoint (alignment point) of the vortices. The mean flow is directed into the plane, i.e. the vortices are viewed from the rear. The configuration of the subplots is identical in all the figures. The right column shows Case 1 vortices with positive streamwise vorticity ω_x (clockwise rotation) and the left column shows Case 2 vortices with negative streamwise vorticity (anti-clockwise rotation). In the top row, the vortices are displayed in the xyz-frame of reference, and in the bottom row, the same vortices are displayed in a frame of reference aligned with the direction of the mean flow ($\theta = 8°$, as suggested in Figure 6). The thick solid line is a contour of negative λ_2, indicating the centre position of the vortices. It should be noted that the coordinate transformation causes the centre of the vortex to be located at different y^+-positions in the two reference frames. The thin solid and dashed lines indicate positive and negative contours, respectively. In each figure the contour increment is constant, implying that the number of contour lines may vary from one subplot to another within that figure.

Figure 13 shows contour plots of ensemble-averaged streamwise velocity fluctuations $\langle u - U \rangle$. The thick contour indicates that the centre of the λ_2-vortex is located at $z^+ \approx 20$. Although the flow patterns generated by Case 1 and Case 2 vortices are generally similar, the plots in the top row indicate that there is a slight asymmetry between the two cases. This asymmetry is retained when the coordinate system is aligned with the direction of the mean flow (bottom row), confirming that for the streamwise velocity component there is a physical effect of the crossflow. As was observed also by Jeong *et al.* [5] for a 2DTBL and by Lygren and Andersson [18] for a three-dimensional turbulent disk flow, the peak in positive $\langle u - U \rangle$ is located closer to the wall than the peak of negative $\langle u - U \rangle$. Lygren and Andersson [18] also observed a reduction of positive fluctuations

DOI: 10.1002/fld

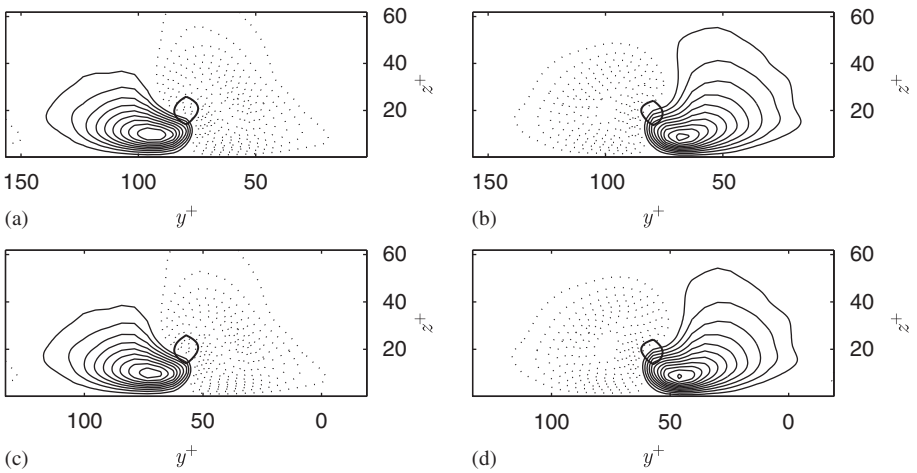

Figure 13. Cross-sectional cut of ensemble-averaged coherent streamwise velocity $\langle u-U\rangle$ with contour increment 0.0094. The mean flow is directed into the plane. The thick solid single contour in the middle of the plot represents the vortex core expressed as negative λ_2, and solid and dotted lines represent positive and negative contours, respectively. (a) Case 2 vortex (anti-clockwise rotation) and no system rotation ($\theta=0°$); (b) Case 1 vortex (clockwise rotation) and no system rotation ($\theta=0°$); (c) Case 2 vortex with system rotation ($\theta=8°$); and (d) Case 1 vortex with system rotation ($\theta=8°$).

relative to negative fluctuations, especially for Case 2 vortices. As can be seen from Figure 13(c) and 13(d) by comparing the number of positive and negative contour lines, this is not the case here.

Figure 14 shows contour plots of ensemble-averaged spanwise velocity fluctuations $\langle v-V\rangle$. The plots in the top row indicate that there is a small asymmetry between the two cases. This asymmetry is not retained (or at least negligible) when the coordinate system is aligned with the direction of the mean flow (bottom row), suggesting that for the spanwise velocity component the effect of the crossflow is negligible. There are some differences in the contour levels closest to zero, but these represent small values and any difference such as shown in the bottom row may not be significant. There are also small differences in the number of contour lines, i.e. reduction of negative fluctuations relative to positive fluctuations (the extreme values are different for vortices of opposite sense of rotation in the bottom row), but the significance of this is uncertain.

Figure 15 shows contour plots of ensemble-averaged wall-normal velocity fluctuations $\langle w\rangle$. As was the case for the streamwise velocity component, the asymmetry between vortices with opposite sense of rotation is retained when the coordinate system is aligned with the direction of the mean flow (bottom row), confirming that for the wall-normal velocity component there is a physical effect of the crossflow. The rotation of the contour line $\langle w\rangle=0$ in the opposite direction of the vortex rotation was observed and explained by Jeong *et al.* [5] for the turbulent channel flow, observed again by Lygren and Andersson [18] in their turbulent disk flow and still again by Solbakken and Andersson [41] in their lubricated channel flow. As can be seen from Figure 15(c) and 15(d), the present flow case also exhibits this rotation of the contour line $\langle w\rangle=0$. Here, the rotation angle relative to the vertical z-axis is distinctly larger for the Case 1 vortex than for the Case 2 vortex. Owing to this tilting, $\partial\langle w\rangle/\partial z<0$ in the vortex core in both cases.

DOI: 10.1002/fld

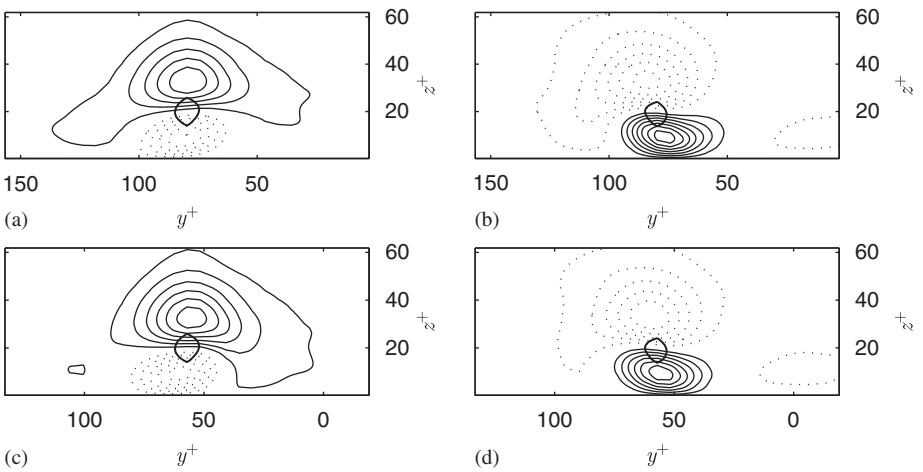

Figure 14. Cross-sectional cut of ensemble-averaged coherent spanwise velocity $\langle v - V \rangle$ with contour increment 0.0102. The plots are otherwise organized as in Figure 13.

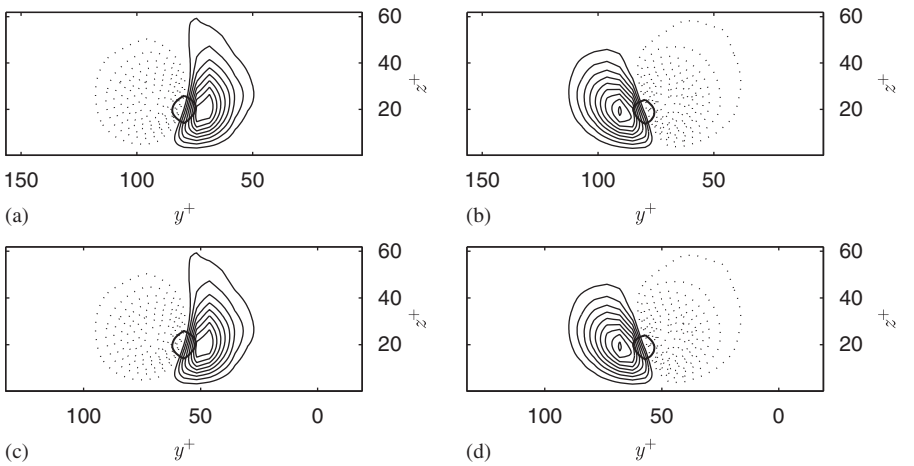

Figure 15. Cross-sectional cut of ensemble-averaged coherent wall-normal velocity $\langle w \rangle$ with contour increment 0.0047. The plots are otherwise organized as in Figure 13.

Figure 16 shows contour plots of the ensemble-averaged Reynolds stress $-\langle u - U \rangle \langle w \rangle$ normalized by the global mean wall shear stress τ_w. Here, nomenclature from the quadrant analysis [42] will be introduced where the primary Reynolds stress component $-\overline{uw}$ is divided into four categories according to the sign of the streamwise and wall-normal velocity fluctuations. First quadrant events (Q1) involve outward motion of high-speed fluid ($u>0, w>0$), second quadrant events (Q2) involve outward motion of low-speed fluid ($u<0,\ w>0$) often referred to as ejection events, third quadrant events (Q3) involve inward motion of low-speed fluid ($u<0, w<0$) and fourth quadrant

DOI: 10.1002/fld

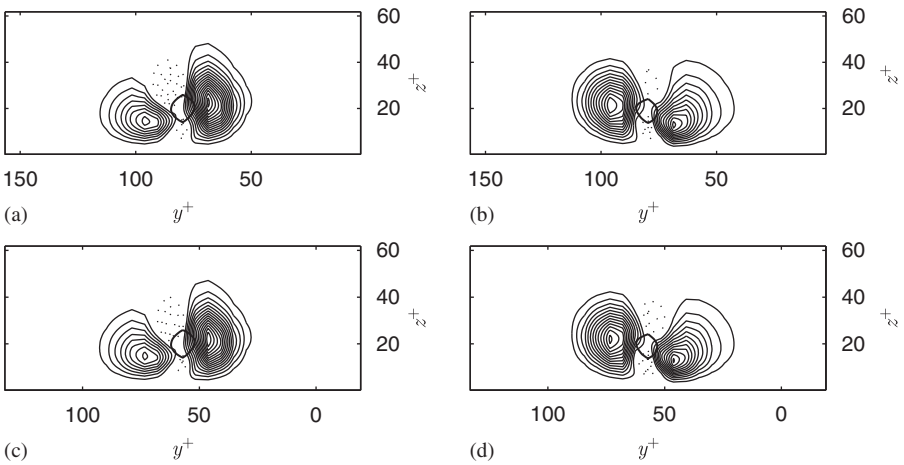

Figure 16. Cross-sectional cut of ensemble-averaged coherent Reynolds stress $-\langle u-U\rangle\langle w\rangle$ normalized by the global mean wall shear stress with contour increment 0.227. The plots are otherwise organized as in Figure 13.

events (Q4) involve inward motion of high-speed fluid ($u>0, w<0$) often referred to as sweep events.

In the xyz-frame of reference (top row) there is an asymmetry between Case 1 and Case 2 vortices, and this asymmetry is retained when the coordinate system is aligned with the direction of the mean flow (bottom row), especially for the contours indicating Q2 and Q4 events, but to some extent also for Q1 and Q3 events. This implies that the asymmetry is not merely a consequence of viewing the vortices in a frame of reference not aligned with the mean flow, but for $-\langle u-U\rangle\langle w\rangle$ there is a distinct physical effect of the crossflow.

Both Lygren and Andersson [18] and Jung and Sung [20] observed a reduction in the contribution of Q4 events relative to Q2 events to the shear stress $-\langle u-U\rangle\langle w\rangle$, especially for Case 2 vortices. Here, we find that for Case 2 vortices, the contribution of Q4 events is only about 50% of the contribution of Q2 events, while the contribution from Q2 and Q4 events are roughly equal for Case 1 vortices. Jung and Sung [20] also noted that the Q4 event related to the Case 2 vortex was weaker than that related to the Case 1 vortex. As can be seen from inspection of Q4 events in Figure 16, this is the case here (the contribution of the Case 1 vortex is about 40% higher than that of the Case 2 vortex). Figure 16 also reveals some small differences between Case 1 and Case 2 vortices regarding Q1 and Q3 events, but these events do not contribute much to the total Reynolds-averaged shear stress $-\langle u-U\rangle\langle w\rangle$.

Figure 17 shows contour plots of ensemble-averaged Reynolds stress $-\langle u-U\rangle\langle v-V\rangle$ normalized by the global mean wall shear stress τ_w. In the xyz-frame of reference (top row) there is an asymmetry between Case 1 and Case 2 vortices, and this asymmetry is partially retained when the coordinate system is aligned with the direction of the mean flow (bottom row). As for the primary stress component, this implies that for $-\langle u-U\rangle\langle v-V\rangle$ there is a physical effect of the crossflow. The most obvious difference between Case 1 and Case 2 vortices in Figure 17 is that the positive contribution of the Case 2 vortex at $z^+\approx 10$ is only about 50% of the negative contribution from the Case 1 vortex at the same wall distance. Also, above the vortex at $z^+\approx 30$ the negative

DOI: 10.1002/fld

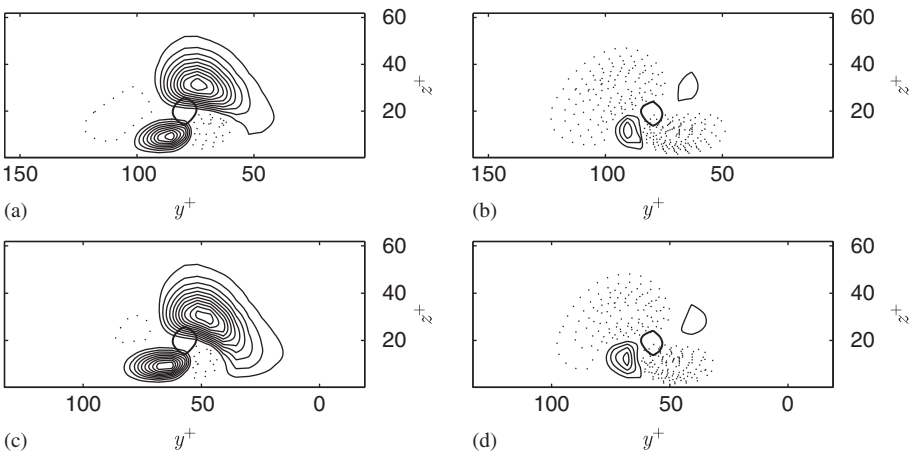

Figure 17. Cross-sectional cut of ensemble-averaged coherent Reynolds stress $-\langle u-U\rangle\langle v-V\rangle$ normalized by the global mean wall shear stress with contour increment 0.372. The plots are otherwise organized as in Figure 13.

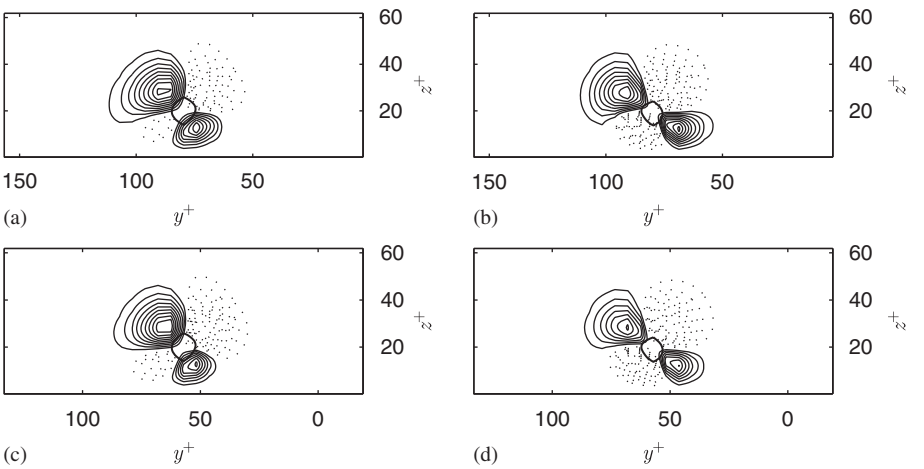

Figure 18. Cross-sectional cut of ensemble-averaged coherent Reynolds stress $-\langle v-V\rangle\langle w\rangle$ normalized by the global mean wall shear stress with contour increment 0.165. The plots are otherwise organized as in Figure 13.

contribution of the Case 1 vortex appears to be somewhat smaller than the positive contribution of the Case 2 vortex.

Figure 18 shows contour plots of ensemble-averaged Reynolds stress $-\langle v-V\rangle\langle w\rangle$ normalized by the global mean wall shear stress τ_w. In the xyz-frame of reference (top row), there is an asymmetry between vortices with opposite sense of rotation, and this asymmetry is still present, but different, when the coordinate system is aligned with the direction of the mean flow (bottom row). This implies that also for this shear stress component there is an effect of the crossflow.

DOI: 10.1002/fld

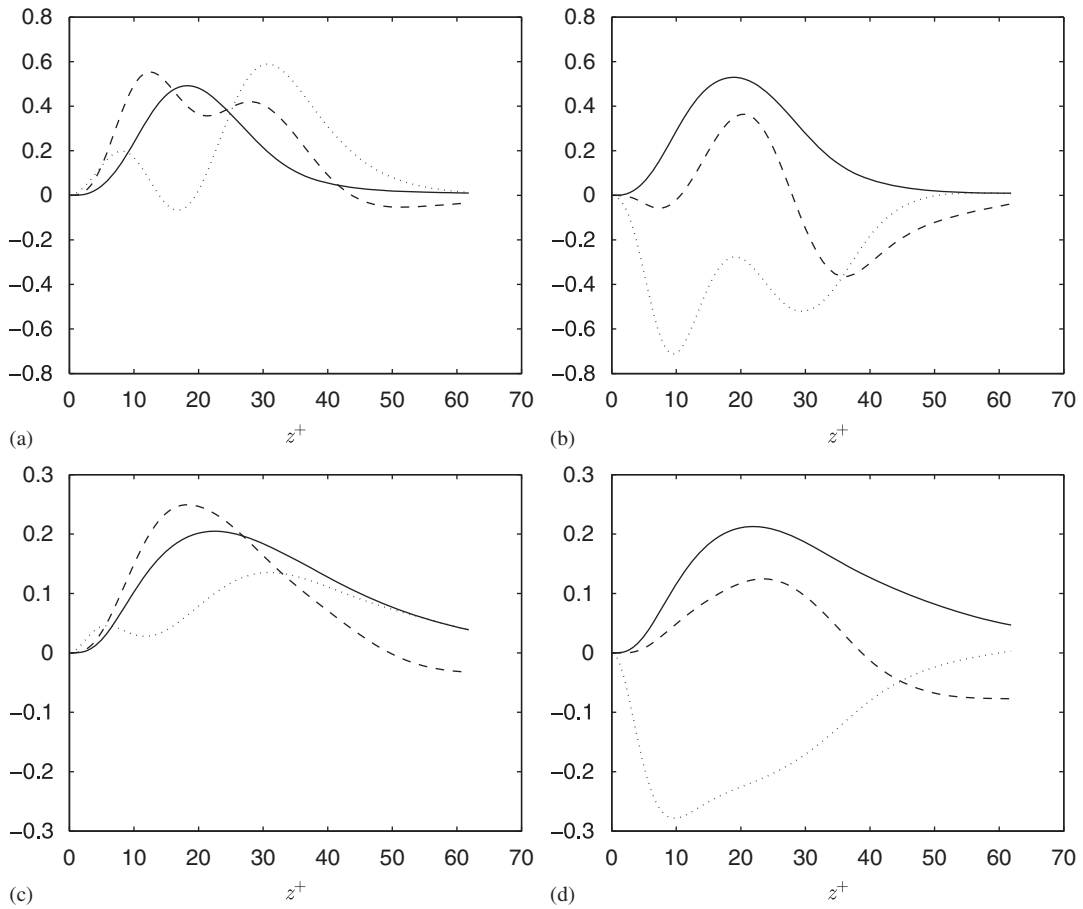

Figure 19. Ensemble-averaged coherent primary shear stress $-\langle u-U\rangle\langle w\rangle$ (——) normalized by τ_{w_x}, secondary shear stress $-\langle v-V\rangle\langle w\rangle$ (- - -) normalized by τ_{w_y} and tertiary shear stress $-\langle u-U\rangle\langle v-V\rangle$ ($\cdots$) normalized by τ_w: (a), (b) stresses in a cross-sectional plane through the midpoint of a Case 2 and Case 1 vortex averaged in the y-direction and (c), (d) stresses around a Case 2 and Case 1 vortex averaged in the x- and y-directions.

In an effort to relate the ensemble-averaged shear stresses associated with the coherent vortices to the global shear stresses averaged in time and in the homogeneous directions, we have averaged the ensemble-averaged stresses $-\langle u-U\rangle\langle w\rangle$, $-\langle u-U\rangle\langle v-V\rangle$ and $-\langle v-V\rangle\langle w\rangle$ shown in Figures 16, 17 and 18 in the y-direction. To further assess the gross effect of the structures and relate them to the global statistics, we have also averaged the ensemble-averaged stresses in both the y- and x-directions. Both these averages are shown in Figure 19 for all the turbulent shear stress components.

Even though the contour plots of $-\langle u-U\rangle\langle w\rangle$ in a cross-sectional plane through the midpoint of the vortices in Figure 16(a) and (b) reveal spatial asymmetries between Case 1 and Case 2 vortices, the gross effect appears to be about equal when the stress in the plane is averaged in the

DOI: 10.1002/fld

y-direction (Figure 19(a) and (b)). As expected, both Case 1 and Case 2 vortices yield positive contributions all the way from the wall to $z^+=60$. The location of the peak value at $z^+\approx 20$ is consistent with the increase of $-\overline{uw}$ in Figure 5(a) throughout the buffer layer. The peak value of $-\langle u-U\rangle\langle w\rangle$ in Figure 19(a) and (b) is also of the same order of magnitude as $-\overline{uw}$ in the buffer layer, strongly suggesting that coherent vortical structures are the primary source of shear stress production in the buffer layer. Averaging in the x-direction, as well as in the y-direction, confirms this picture as can be seen in Figure 19(c) and (d). The gross effects of Case 1 and Case 2 vortices are about equal and the peak is still located at $z^+\approx 20$. The distribution is broader and the peak value is reduced, probably because of the inclination of the vortices.

For $-\langle u-U\rangle\langle v-V\rangle$, the contribution from Case 1 vortices appears to be rather different from that of Case 2 vortices. As expected from inspection of Figure 17(a) and (b), Case 1 vortices make a negative contribution to $-\overline{uv}$, whereas Case 2 vortices make a positive contribution. The Case 1 vortex produces a minimum at $z^+\approx 10$, most clearly displayed when the stress is averaged also in the x-direction (Figure 17(c) and (d)). The distinct minimum produced by the Case 1 vortex along with the modest positive contribution of the Case 2 vortex is fully consistent with the minimum of $-\overline{uv}$ at $z/h\approx 0.125(z^+\approx 10)$ and the subsequent increase towards zero in the range $0.125<z/h<1$ in Figure 5(b).

At first sight, the secondary shear stress $-\overline{vw}$ in Figure 5(b) can hardly be related to the ensemble-average $-\langle v-V\rangle\langle w\rangle$ in Figure 18. Lygren and Andersson [18] also reported small spatial averages for the secondary shear stress component, and concluded that it was difficult to relate the educed near-wall structure to the global secondary shear stress. A closer look at the contour plots in Figure 18 reveals a net positive contribution underneath the Case 2 vortex, whereas the net contribution from the Case 1 vortex appears to be quite small. In Figure 19 the non-zero spatial average of $-\langle v-V\rangle\langle w\rangle$ is clearly seen. Case 1 vortices seem to make both positive and negative contributions, whereas Case 2 vortices predominantly make positive contributions. The contribution from the Case 2 vortex is substantially larger than the contribution from the Case 1 vortex, but both vortices produce a maximum at $z^+\approx 20$, corresponding to the position of the maximum in Figure 5(b).

In 2DTBLs, both the secondary and tertiary shear stresses, denoted by $-\langle v-V\rangle\langle w\rangle$ and $-\langle u-U\rangle\langle v-V\rangle$ in the present study, have spatial distributions, but the average when vortices of both signs are included is negligible, cf. Jeong *et al.* [5]. The present investigation of the spatial distribution of the coherent shear stresses and the wall-normal variation of these stresses when averaged in the x- and y-directions (Figure 19) bring evidence that all three turbulent shear stress components can be related to the same near-wall coherent structure. This observation thus reinforces the hypothesis of Eaton [2] that the structural model for 2DTBLs proposed by Robinson [4], and later refined by Jeong *et al.* [5], is valid also for 3DTBLs.

5.4. Skin friction pattern

The skin friction pattern underneath coherent near-wall structures has previously been investigated by Solbakken and Andersson [43] in a plane pressure-driven two-dimensional channel flow. As in the present study, they extracted the vortices using the λ_2 vortex definition and ensemble-averaged the surrounding flow field according to the scheme devised by Jeong *et al.* [5]. High levels of skin friction are believed to be caused by the sweep motion induced by the near-wall structures as high-speed fluid is swept towards the wall. Solbakken and Andersson [43] confirmed this conjecture, and also found that the maximum skin friction occurs near the tail of the structure and not aside

DOI: 10.1002/fld

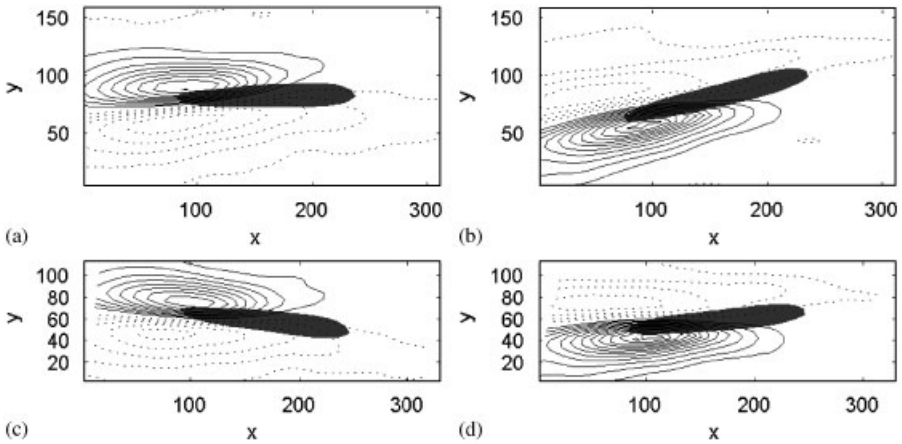

Figure 20. Top view of ensemble-averaged coherent skin friction $\tau_{w_x} = \mu \mathrm{d}U/\mathrm{d}z|_{z=0}$ normalized by the global mean wall shear stress. The global mean flow U is from left to right. Solid and dotted lines represent values larger and smaller than the mean, respectively. The shaded region shows an isosurface of non-dimensional $\lambda_2 = -0.012$. The contour increment for the stresses is 0.063 in all plots. In this plot x and y denote the wall coordinates (normally denoted x^+ and y^+) in the streamwise and spanwise directions, respectively. The plots are otherwise organized as in Figure 13.

the midpoint of the structure. They therefore concluded that the proximity of the vortex tail to the wall outweighs the higher levels of streamwise vorticity at the midpoint in generating high levels of skin friction. Here, we want to investigate whether the skin friction pattern reported by Solbakken and Andersson [43] is changed due to the mean three-dimensionality imposed by the crossflow.

Figure 20 shows the skin friction $\tau_{w_x} = \mu \mathrm{d}U/\mathrm{d}z|_{z=0}$ normalized by the global mean wall shear stress τ_w beneath the educed coherent structure. Generally, the skin friction pattern of this 3DTBL appears to be very similar to that reported by Solbakken and Andersson [43] for a 2DTBL, regardless of whether the friction is expressed in the xyz-frame of reference or in a coordinate system aligned with the direction of the mean flow. There are however some observations to be made. In the xyz-frame of reference (top row), the Case 1 vortex seems to produce a slightly higher maximum value than the Case 2 vortex. When the coordinate system is aligned with the direction of the mean flow (bottom row), the maximum value of the Case 1 vortex is 50% higher than that of the Case 2 vortex. The value of the minimum skin friction on the other hand seems to be unaffected by the coordinate transformation.

As was reported by Solbakken and Andersson [43] for a 2DTBL, the maximum skin friction in the present case is located close to the vortex tail on the sweep side. The region of high skin friction is also long and narrow and approximately of the same size as the educed structure itself. Solbakken and Andersson [43] reported the distance from the maximum skin friction to the midpoint of the vortex to be $x^+ \approx 80$ and $y^+ \approx 18$ in the streamwise and spanwise direction, respectively. In the present case, the corresponding distances are $x^+ \approx 60$ and $y^+ \approx 20$. The region of low skin friction is located on the ejection side of the vortex, also close to the tail, and covers a larger area than the region of high friction. Solbakken and Andersson [43] found that the maximum skin friction

DOI: 10.1002/fld

exceeded the global mean skin friction τ_w by 50%, whereas the minimum skin friction was only 25% below the mean. Here, the corresponding numbers are very similar.

6. SUMMARY AND CONCLUDING REMARKS

An equilibrium 3DTBL has been generated by the imposition of a spanwise pressure gradient on an already fully developed turbulent plane Couette flow. The flow has been studied numerically by DNS. The results show that the variation of the direction of the mean flow with the wall-normal distance is modest, while the non-alignment of the shear stress and velocity gradient angles in planes parallel to the wall indicates distinct three-dimensionality. The results also show that the value of the structure parameter a_1 is slightly larger than that of the two-dimensional reference case throughout the near-wall region, indicating that the ability of a given amount of turbulent shear stress to produce and sustain turbulent kinetic energy may actually be larger in 3DTBLs than in 2DTBLs. Jung and Sung [20] made the same observation in their study of a similar flow, contrary to what is typically found in 3DTBLs, e.g. Eaton [2].

Near-wall turbulent structures have been studied using the λ_2 vortex definition. One-point λ_2 statistics, isosurfaces of instantaneous negative λ_2 and ensemble-averaging of selected vortices reveal that the near-wall structures of this flow are similar, but not identical, to those found in 2DTBLs, cf. Jeong *et al.* [5] and in other equilibrium 3DTBLs, cf. Lygren and Andersson [18] and Jung and Sung [20]. The fact that there is an asymmetry between Case 1 and Case 2 vortices, both in the xyz-frame of reference and in the alternative frame of reference aligned with the direction of the local mean flow, brings evidence that the near-wall structures are indeed affected by the mean three-dimensionality. However, the observed asymmetries are distinctly different in the two frames of reference, suggesting that the choice of reference may influence the results and the conclusions drawn. Aligning the alternative frame of reference with the direction of the local mean flow seemed natural here since the observed 8°-turning of the mean-flow vector remained practically constant across the flow. In other flows, the choice of an alternative frame of reference may be less obvious. This may explain why the majority of earlier studies of 3DTBLs resorted to reference frames aligned with the direction of the primary flow.

The role of coherent near-wall structures in generating turbulent shear stress is well documented in 2DTBLs. The ensemble-averaged shear stresses, averaged in the x- and y-directions (Figure 19) confirm and reinforce this understanding by providing a direct link between the flow field surrounding ensemble-averaged near-wall structures and global (i.e. Reynolds-averaged) statistics. The location and magnitude of the peak values and the wall-normal variation of all three shear stress components have been related to and explained by the educed near-wall structures through Figure 19. The fact that the secondary and tertiary shear stresses can be related to the same near-wall structures as the primary shear stress brings evidence that one set of coherent structures, though somewhat altered by mean-flow three-dimensionality, is responsible for the production of all three shear stress components. These observations reinforce the hypothesis of Eaton [2] that the structural model for 2DTBLs proposed by Robinson [4], and later refined by Jeong *et al.* [5], is valid also for 3DTBLs.

Finally, the skin friction pattern underneath the near-wall coherent structures appears to be similar to that of a 2DTBL, although some differences in the patterns generated by Case 1 and Case 2 vortices are observed.

DOI: 10.1002/fld

In summary, the imposition of a moderate sideways pressure gradient onto the otherwise unidirectional shear-driven Couette flow gives rise to:

1. a ca 8°-turning of the mean velocity vector away from the Couette flow direction,
2. a corresponding turning of the coherent near-wall vortices,
3. a breaking of the conventional symmetry between Case 1 and Case 2 vortices.

The first two effects give rise to secondary and tertiary shear stresses. The observed symmetry-breaking of the coherent vortices adds a further complexity to the flow topology and tends to explain why turbulence models aimed at 2DTBLs often fail in computations of 3DTBLs.

Unlike most other 3DTBLs considered before, the present Couette–Poiseuille flow is statistically stationary and homogeneous in planes parallel to the walls. This is a particularly attractive feature since Reynolds-averaged momentum equations and one-point turbulence model equations then reduce to a coupled set of ordinary differential equations in the wall-normal coordinate. This advantageous feature is shared by the 3DTBL studied recently by Jung and Sung [20], but the present flow is not affected by the centrifugal body forces and wall curvature. It is therefore believed that the Couette–Poiseuille flow studied in the present paper, with its full Reynolds stress tensor, constitutes a valuable and yet clear-cut test case to assist the striving towards more realistic turbulence models aimed at computations of three-dimensional shear flows.

The conclusions arrived at in this paper are based on results from a flow with relatively weak mean three-dimensionality, in which the imposed lateral pressure gradient turned the mean-flow vector about 8°. The present findings are believed to be representative also for other 3DTBLs with moderate mean three-dimensionality, but not necessarily for severely skewed 3DTBLs.

ACKNOWLEDGEMENTS

This work has received support from The Research Council of Norway (Programme for Supercomputing) through a grant of computing time.

REFERENCES

1. Bradshaw P. Turbulent secondary flows. *Annual Review of Fluid Mechanics* 1987; **19**:53–74.
2. Eaton JK. Effects of mean flow three dimensionality on turbulent boundary-layer structure. *AIAA Journal* 1995; **33**:2020–2025.
3. Johnston JP, Flack KA. Review: advances in three-dimensional turbulent boundary layers with emphasis on the wall-layer regions. *Journal of Fluids Engineering* 1996; **118**:219–232.
4. Robinson SK. Coherent motions in the turbulent boundary layer. *Annual Review of Fluid Mechanics* 1991; **23**:601–639.
5. Jeong J, Hussain F, Schoppa W, Kim J. Coherent structures near the wall in a turbulent channel flow. *Journal of Fluid Mechanics* 1997; **332**:185–214.
6. Moin P, Shih T-H, Driver D, Mansour NN. Direct numerical simulation of a three-dimensional turbulent boundary layer. *Physics of Fluids A* 1990; **2**:1846–1853.
7. Sendstad O, Moin P. On the mechanics of 3-D turbulent boundary layers. *Eighth Symposium on Turbulent Shear Flows*, Munich, Germany, 1991; 5-4-1–5-4-5.
8. Coleman GN, Kim J, Le A-T. A numerical study of three-dimensional wall-bounded flows. *International Journal of Heat and Fluid Flow* 1996; **17**:333–342.
9. Le A-T, Coleman GN, Kim J. Near-wall turbulence structures in three-dimensional boundary layers. *Proceedings of the First International Symposium on Turbulence and Shear Flow Phenomena*, Santa Barbara, CA, U.S.A., 1999; 151–156.
10. Le A-T, Coleman GN, Kim J. Near-wall turbulence structures in three-dimensional boundary layers. *International Journal of Heat and Fluid Flow* 2000; **21**:480–488.

DOI: 10.1002/fld

11. Coleman GN, Kim J, Spalart PR. A numerical study of strained three-dimensional wall-bounded turbulence. *Journal of Fluid Mechanics* 2000; **416**:75–116.
12. Bradshaw P, Pontikos NS. Measurements in the turbulent boundary layer on an 'infinite' swept wing. *Journal of Fluid Mechanics* 1985; **159**:105–130.
13. Schwarz WR, Bradshaw P. Turbulence structural changes for a three-dimensional turbulent boundary layer in a 30° bend. *Journal of Fluid Mechanics* 1994; **272**:183–209.
14. Littell HS, Eaton JK. Turbulence characteristics of the boundary layer on a rotating disk. *Journal of Fluid Mechanics* 1994; **266**:175–207.
15. Kang HS, Choi H, Yoo JY. On the modification of the near-wall coherent structure in a three-dimensional turbulent boundary layer on a free rotating disk. *Physics of Fluids* 1998; **10**:2315–2322.
16. Flack KA. Near-wall structure of three-dimensional turbulent boundary layers. *Experiments in Fluids* 1997; **23**:335–340.
17. Wu X, Squires KD. Prediction and investigation of the turbulent flow over a rotating disk. *Journal of Fluid Mechanics* 2000; **418**:231–264.
18. Lygren M, Andersson HI. Turbulent flow between a rotating and a stationary disk. *Journal of Fluid Mechanics* 2001; **426**:297–326.
19. Jeong J, Hussain F. On the identification of a vortex. *Journal of Fluid Mechanics* 1995; **285**:69–94.
20. Jung SY, Sung HJ. Characterization of the three-dimensional turbulent boundary layer in a concentric annulus with a rotating inner cylinder. *Physics of Fluids* 2006; **18**:1–11. Art. No. 115102.
21. Randriamampianina A, Poncet S. Turbulence characteristics of the Bödewadt layer in a large enclosed rotor–stator system. *Physics of Fluids* 2006; **18**:1–16. Art. No. 055104.
22. Poncet S, Randriamampianina A. Three-dimensional turbulent boundary layer in a shrouded rotating system. *Flow, Turbulence and Combustion* 2008; **80**:107–117.
23. Spalart PR. Theoretical and numerical study of a three-dimensional turbulent boundary layer. *Journal of Fluid Mechanics* 1989; **205**:319–340.
24. Coleman GN, Ferziger JH, Spalart PR. A numerical study of the turbulent Ekman layer. *Journal of Fluid Mechanics* 1990; **213**:313–348.
25. Wu X, Squires KD. Large eddy simulation of an equilibrium three-dimensional turbulent boundary layer. *AIAA Journal* 1997; **35**:67–74.
26. Orlandi P, Fatica M. Direct simulations of turbulent flow in a pipe rotating about its axis. *Journal of Fluid Mechanics* 1997; **343**:43–72.
27. Orlandi P. Helicity fluctuations and turbulent energy production in rotating and non-rotating pipes. *Physics of Fluids* 1997; **9**:2045–2056.
28. Kannepalli C, Piomelli U. Large-eddy simulation of a three-dimensional shear-driven turbulent boundary layer. *Journal of Fluid Mechanics* 2000; **423**:175–203.
29. Kiesow RO, Plesniak MW. Modification of near-wall structure in a shear-driven 3-D turbulent boundary layer. *Journal of Fluids Engineering* 2002; **124**:118–126.
30. Kiesow RO, Plesniak MW. Near-wall physics of a shear-driven three-dimensional turbulent boundary layer with varying crossflow. *Journal of Fluid Mechanics* 2003; **484**:1–39.
31. Tennekes H, Lumley JL. *A First Course in Turbulence*. The MIT Press: Cambridge, MA, 1972.
32. Bech KH, Tillmark N, Alfredsson PH, Andersson HI. An investigation of turbulent plane Couette flow at low Reynolds numbers. *Journal of Fluid Mechanics* 1995; **286**:291–325.
33. Manhart M. A zonal grid algorithm for DNS of turbulent boundary layers. *Computers and Fluids* 2004; **33**:435–461.
34. Bech KH, Andersson HI. Very-large-scale structures in DNS. *Direct and Large-Eddy Simulation I*. Kluwer Academic Publishers: Dordrecht, The Netherlands, 1994; 13–24.
35. Komminaho J, Lundbladh A, Johansson A. Very large structures in plane turbulent Couette flow. *Journal of Fluid Mechanics* 1996; **320**:259–285.
36. Hu Z, Morfey CL, Sandham ND. Aeroacoustics of wall-bounded turbulent flows. *AIAA Journal* 2002; **40**:465–473.
37. Hu Z, Morfey CL, Sandham ND. Sound radiation in turbulent channel flows. *Journal of Fluid Mechanics* 2003; **475**:269–302.
38. Tsukahara T, Kawamura H, Shingai K. DNS of turbulent Couette flow with emphasis on the large-scale structure in the core region. *Journal of Turbulence* 2006; **7**:1–16.
39. Holstad A, Johansson PS, Andersson HI, Pettersen B. On the influence of domain size on POD modes in turbulent plane Couette flow. *Direct and Large-Eddy Simulation VI*. Springer: Dordrecht, The Netherlands, 2006:763–770.

DOI: 10.1002/fld

40. Shizawa T, Eaton JK. Turbulence measurements for a longitudinal vortex interacting with a three-dimensional turbulent boundary layer. *AIAA Journal* 1992; **30**:49–55.
41. Solbakken S, Andersson HI. Direct numerical simulation of lubricated channel flow. *Fluid Dynamics Research* 2005; **37**:203–230.
42. Willmarth WW, Lu SS. Structure of Reynolds stress near the wall. *Journal of Fluid Mechanics* 1972; **55**:65–92.
43. Solbakken S, Andersson HI. The generic skin-friction pattern underneath coherent near-wall structures. *Fluid Dynamics Research* 2004; **34**:167–174.

DOI: 10.1002/fld